TOPICAL REVIEW — Magnetism, magnetic materials, and interdisciplinary research

Dynamics of magnetization in ferromagnet with spin-transfer torque*

Li Zai-Dong(李再东)[a)†], He Peng-Bin(贺鹏斌)[b)], and Liu Wu-Ming(刘伍明)[c)]

[a)] Department of Applied Physics, Hebei University of Technology, Tianjin 300401, China

[b)] College of Physics and Microelectronics Science, Key Laboratory for Micro-Nano Physics and Technology of Hunan Province, Hunan University, Changsha 410082, China

[c)] Beijing National Laboratory for Condensed Matter Physics, Institute of Physics, Chinese Academy of Sciences, Beijing 100190, China

(Received 26 July 2014; published online 24 September 2014)

We review our recent works on dynamics of magnetization in ferromagnet with spin-transfer torque. Driven by constant spin-polarized current, the spin-transfer torque counteracts both the precession driven by the effective field and the Gilbert damping term different from the common understanding. When the spin current exceeds the critical value, the conjunctive action of Gilbert damping and spin-transfer torque leads naturally the novel screw-pitch effect characterized by the temporal oscillation of domain wall velocity and width. Driven by space- and time-dependent spin-polarized current and magnetic field, we expatiate the formation of domain wall velocity in ferromagnetic nanowire. We discuss the properties of dynamic magnetic soliton in uniaxial anisotropic ferromagnetic nanowire driven by spin-transfer torque, and analyze the modulation instability and dark soliton on the spin wave background, which shows the characteristic breather behavior of the soliton as it propagates along the ferromagnetic nanowire. With stronger breather character, we get the novel magnetic rogue wave and clarify its formation mechanism. The generation of magnetic rogue wave mainly arises from the accumulation of energy and magnons toward to its central part. We also observe that the spin-polarized current can control the exchange rate of magnons between the envelope soliton and the background, and the critical current condition is obtained analytically. At last, we have theoretically investigated the current-excited and frequency-adjusted ferromagnetic resonance in magnetic trilayers. A particular case of the perpendicular analyzer reveals that the ferromagnetic resonance curves, including the resonant location and the resonant linewidth, can be adjusted by changing the pinned magnetization direction and the direct current. Under the control of the current and external magnetic field, several magnetic states, such as quasi-parallel and quasi-antiparallel stable states, out-of-plane precession, and bistable states can be realized. The precession frequency can be expressed as a function of the current and external magnetic field.

Keywords: spin-transfer torque, domain wall, soliton, ferromagnetic resonance

PACS: 75.60.Ch, 72.25.Ba, 75.78.–n, 75.40.Gb **DOI:** 10.1088/1674-1056/23/11/117502

1. Introduction

In solid physics, the Heisenberg model of spin–spin interactions can be considered as the starting point for understanding the complex magnetic structures. This model has successfully explained the existence of ferromagnetism and antiferromagnetism below the Curie temperature, and also attracted considerable attention in nonlinear science and condensed-matter physics.[1] The state of a magnetic crystal is unambiguously described by the magnetization vector $\boldsymbol{M}$, and the dynamics and kinetics of a ferromagnet is dictated by variations in its magnetization. The magnetization of a ferromagnet as a function of space and time obeys the Landau–Lifshitz–Gilbert equation[2–5]

$$\frac{\partial \boldsymbol{M}}{\partial t} = -\gamma \boldsymbol{M} \times \boldsymbol{H}_{\text{eff}} + \frac{\alpha}{M_{\text{s}}} \boldsymbol{M} \times \frac{\partial \boldsymbol{M}}{\partial t}, \tag{1}$$

where $\boldsymbol{M} \equiv \boldsymbol{M}(x,t)$ is the localized magnetization, γ is the gyromagnetic ratio, α is the damping parameter, M_{s} is the saturation magnetization, and $\boldsymbol{H}_{\text{eff}}$ represents the effective magnetic field including the external field, the anisotropy field, the demagnetization field, and the exchange field. Equation (1) governs a classical nonlinear dynamical system with novel properties.

Because of attraction, a cluster of magnons in ferromagnet tends to be self-localization. In a certain sense, the attraction of magnons is critical for a one-dimensional ferromagnet because it produces a bound state of quasi-particles (magnons), i.e., self-localization. A spin wave may be regarded as a cluster of a macroscopic number of coherent magnons. The magnon cluster tends to be localized, and thus the spin wave becomes unstable. The developing instability causes magnetization localization and brings about topological soliton (domain wall) and dynamic soliton.[3] A magnetic domain wall can be understood as a potential hill which separates two generated magnetic states. It forms a spatially localized configuration of magnetization in ferromagnet and the

*Project supported by the Natural Science Foundation of Hebei Province of China (Grant No. A2012202022). P. B. He was supported by the Aid Program for Young Teachers of Hunan University, the Project-sponsored by SRF for ROCS, SEM, and the Aid Program for Science and Technology Innovative Research Team in Higher Educational Institution of Hunan Province, China. W. M. Liu was supported by the National Basic Research Program of China (Grant Nos. 2011CB921502 and 2012CB821305) and the National Natural Science Foundation of China (Grant Nos. 61227902 and 61378017).

†Corresponding author. E-mail: lizd2018@live.com

© 2014 Chinese Physical Society and IOP Publishing Ltd

direction of magnetic moments inverses gradually. On the other hand, the dynamic soliton describes the localized states of magnetization which can be reduced to a uniform magnetization by continuous deformation, so that the excited ferromagnet transites to the ground state. Therefore, a dynamic soliton is sometimes said to be topologically equivalent to the ground state.

Driven by the constant forces, such as magnetic field[6,7] or spin-polarized current,[8–10] the dynamical motion of magnetization can be described generally by the famous Landau–Lifshitz–Gilbert equation[5] or the modified Landau–Lifshitz–Gilbert equation with spin-transfer torque.[11–14] In these nonlinear equations time only plays the role of an independent variable and does not appear explicitly in the coefficients. Nowadays, the corresponding solutions are called autonomous magnetic domain wall or soliton solutions which are similar to the classical soliton concept introduced firstly by Zabusky and Kruskal[15] for autonomous nonlinear and dispersive dynamic systems.[16] These autonomous solitons can completely preserve their localized form and speed during propagation which has motivated great attention in optical fibers and condensate physics. The field driven autonomous domain wall motion has been studied extensively in thin films[17] and recently in magnetic nanowires[18–23] which has technological application in race track memory.[24] The domain wall travelling speed in magnetic materials conventionally depends on the strength of a constant magnetic field below the Walker breakdown value.[6,7] Above this critical value, the domain wall develops a complex internal structure with temporal dependence which results in domain wall velocity oscillation.[18,19,25,26]

Another autonomous motion of magnetization is formed by passing the constant spin-polarized current across the ferromagnetic nanowire. When a spin-polarized electric current flows through domain wall, the spin polarization of conduction electrons can transfer spin momentum to the local magnetization, thereby applying spin-transfer torque which can manipulate the magnetic domain wall without the applied magnetic field. This spin-transfer effect was theoretically proposed by Slonczewski and Berger,[8] and subsequently verified experimentally.[27] The study of magnetoelectronics has received considerable interest for its technological potential application. In metallic ferromagnets, the differences between electronic bands and scattering cross-sections of impurities for majority and minority spins at the Fermi energy cause spin-dependent mobilities.[28] The difference between spin-up and spin-down electric currents is called a spin current. It is a tensor, with a direction of flow and a spin polarization parallel to the equilibrium magnetization vector $\boldsymbol{M}(\boldsymbol{r},t)$ as,[29] $\mathcal{J} = P\mu_B/(eM_s)\,\boldsymbol{j}_e \otimes \boldsymbol{M}(\boldsymbol{r},t)$, where P is the spin polarization of current, μ_B is the Bohr magneton, and e is the magnitude of electron charge. The vector $\boldsymbol{j}_e$ tracks the direction of the charge current, $\boldsymbol{M}(\boldsymbol{r},t)$ describes the direction of the spin polarization of the current, and M_s is the saturation magnetization. For simpleness, we consider an infinitely long ferromagnetic nanowire where the electronic current flows along the long length of the wire, defined as x direction. Assuming the magnetization is nonuniform only along the direction of current, the spin current can be written as $\boldsymbol{j}(x,t) = b_J \boldsymbol{M}(x,t)$, where $b_J = P j_e \mu_B/(eM_s)$. The spatial variation of the spin current produces a reaction torque on the magnetization as $\boldsymbol{\tau}_b \equiv \partial \boldsymbol{j}/\partial x = b_J \partial \boldsymbol{M}/\partial x$ which enters the modified Landau–Lifshitz equation. As a theoretical model, the modified Landau–Lifshitz–Gilbert equation[11–14] with spin-transfer torque was derived to describe such current-induced magnetization dynamics in a fully polarized ferromagnet. With these novel forms of spin torque, many interesting phenomena have been studied, such as spin wave excitation and instability,[11,30–32] magnetization switching and reversal,[33–36] and magnetic solitons.[37–39] This current-induced magnetization motion exhibits different characteristics from that driven by an magnetic field, and the spin-transfer torque can induce not only precession but also damping role for the motion of magnetization. For the smooth domain wall, this spin torque can displace domain wall opposite to the current direction which has been confirmed experimentally in magnetic thin films and magnetic wires.[40–44]

With the remarkable experimental success measuring the motion of domain wall under the influence of current pulse, considerable progress has been made to understand the current-induced domain wall motion in magnetic nanowire.[12–14,41–48] These studies have improved the pioneering work of current-driven domain wall motion by Berger.[49,50] The dynamics of magnetization described by the Landau–Lifshitz–Gilbert equation admits the static solutions for domain wall motion. In the presence of spin torque and the external magnetic field, it is difficult to derive the dynamic solutions. A circumvented approach is Walker solution analysis[6] for the moving domain wall in response to a steady magnetic field smaller than some critical value. However, this approximation applying to domain wall motion driven by the electric current is unclear, and its reliability has to be verified theoretically and numerically.

When various external time-dependent forces are applied to the physical system, the nonautonomous nonlinear evolution models typically arise and the term of nonautonomous solitons[16] was introduced firstly. Some nonautonomous models and the controllable soliton solutions have been studied theoretically in optical fibers[51] and Bose-Einstein condensates.[52] In ferromagnetic nanowire, this nonautonomous model can be realized by applying the time-dependent magnetic field or current to local magnetization. Such nonautonomous motion of magnetization possesses the

novel character[53–55] which results in the fast domain wall propagation with an optimal field or current pulse.

In the following, we will investigate current driven dynamics of magnetization in ferromagnet. The paper is organized as follows. In Section 2, we investigate the domain wall dynamics in ferromagnetic nanowire driven by spin-polarized current. In Section 3, we expatiate the current-driven dynamic soliton solutions in ferromagnetic nanowire. Section 4 discusses the ferromagnetic resonance in magnetic trilayers with spin torque. Section 5 presents our conclusion.

2. Current driven dynamics of domain wall

A magnetic domain wall is a spatially localized configuration of magnetization in ferromagnet, in which the direction of magnetic moments inverses gradually. When a spin-polarized electric current flows through domain wall, the spin polarization of conduction electrons can transfer spin momentum to the local magnetization, thereby applying spin-transfer torque which can manipulate the magnetic domain wall without the applied magnetic field.

2.1. Domain-wall resonance induced by spin-polarized current

We consider a ferromagnetic metallic film in the xy plane, with the easy axis z perpendicular to the film, as shown in Fig. 1. An in-plane current along the x direction goes through the film. This current exerts spin-transfer torque on the local magnetization. In the presence of adiabatic and non-adiabatic spin-transfer torque, the generalized Landau–Lifshitz–Gilbert equation describing dynamics of magnetization in film can be written as

$$\frac{\partial \boldsymbol{M}}{\partial t} = \gamma \boldsymbol{M} \times \frac{\delta \mathcal{H}}{\delta \boldsymbol{M}} + \frac{\alpha}{M_\mathrm{s}} \boldsymbol{M} \times \frac{\partial \boldsymbol{M}}{\partial t} + \boldsymbol{T}_\mathrm{a} + \boldsymbol{T}_n, \tag{2}$$

where $\mathcal{H}$ is the energy density. The adiabatic spin torque $\boldsymbol{T}_\mathrm{a}$ is caused by the non-equilibrium conduction electrons whose polarizations coincide with the local moments, where $\boldsymbol{T}_\mathrm{a} = -\left[b_\mathrm{J}/\left(1+\xi^2\right)M_\mathrm{s}^2\right]\boldsymbol{M}\times(\boldsymbol{M}\times(\partial \boldsymbol{M}/\partial x))$. Here $\xi = \tau_\mathrm{ex}/\tau_\mathrm{sf}$, $\tau_\mathrm{ex} = \hbar/J_\mathrm{ex}$, J_ex is the s–d exchange coupling strength, τ_sf is the spin-flip relaxation time, and j_e is the electric current density. The adiabatic and non-adiabatic spin torque, i.e., $\boldsymbol{T}_n = -\left[b_\mathrm{J}\xi/\left(1+\xi^2\right)M_\mathrm{s}\right]\boldsymbol{M}\times(\partial \boldsymbol{M}/\partial x)$, is the effect of the non-equilibrium conductive electrons whose polarizations deviate from the local moments.

Taking into account $\boldsymbol{M}^2 = M_\mathrm{s}^2 = \text{const}$ below the Curie temperature, equation (2) can be transformed into two coupled equations for the polar angle θ and azimuth angle ϕ defined relative to the z axis

$$\begin{aligned} &\frac{\partial \theta}{\partial t} + \alpha \frac{\partial \phi}{\partial t}\sin\theta \\ &= -\frac{\gamma}{M_\mathrm{s}\sin\theta}\frac{\delta \mathcal{H}}{\delta \phi} + \frac{b_\mathrm{J}}{1+\xi^2}\left(\frac{\partial \theta}{\partial x} + \xi \frac{\partial \phi}{\partial x}\sin\theta\right), \end{aligned}$$

$$\begin{aligned} &\frac{\partial \phi}{\partial t}\sin\theta - \alpha \frac{\partial \theta}{\partial t} \\ &= \frac{\gamma}{M_\mathrm{s}}\frac{\delta \mathcal{H}}{\delta \theta} + \frac{b_\mathrm{J}}{1+\xi^2}\left(\frac{\partial \phi}{\partial x}\sin\theta - \xi \frac{\partial \theta}{\partial x}\right). \end{aligned} \tag{3}$$

We introduce the dynamic wall structure as follows:[6,56]

$$\theta(x,t) = 2\arctan\exp\left[\frac{x-L(t)}{\Delta(t)}\right], \quad \phi = \phi(t), \tag{4}$$

where $\Delta(t)$ represents the wall width, and $L(t)$ is the normal-displacement coordinate of the wall. For the case of non-zero current, we assume that the wall-magnetization angle ϕ is independent of x. In general, $\Delta(t)$ varies less than $L(t)$, namely, the distortion of wall width is small during the wall motion, $|\mathrm{d}\Delta/\mathrm{d}t| \ll |\mathrm{d}L/\mathrm{d}t|$. Substituting Eq. (4) into Eq. (3), we obtain

$$\frac{\partial L}{\partial t} = 2\pi\gamma M_\mathrm{s}\Delta\sin 2\phi + \alpha\Delta\frac{\partial \phi}{\partial t} - \frac{b_\mathrm{J}}{1+\xi^2}, \tag{5}$$

$$\frac{\partial \phi}{\partial t} = -\gamma\frac{8\pi M_\mathrm{s}}{l_\mathrm{W}}L - \alpha\Delta^{-1}\frac{\partial L}{\partial t} - \frac{b_\mathrm{J}\xi}{1+\xi^2}\Delta^{-1}, \tag{6}$$

where l_W is the length of one domain. The non-adiabatic torques generate global pressure on the walls due to the reigning momentum transfer for the non-adiabatic electrons.[12] The instantaneous pressure arises from the applied field and magnetostatic restoring potential. We assume that at $t = 0$ the current and perpendicular magnetic field is applied and the wall lies in the pinning center. Then, from Eqs. (5) and (6), the initial velocity of wall is $-(1+\alpha\xi)b_\mathrm{J}/\left[\left(1+\xi^2\right)\left(1+\alpha^2\right)\right]$. Like the driving field, both non-adiabatic and adiabatic torque give an initial velocity to the domain wall, but the former is damped. Also, ϕ starts precessing at the Larmor frequency $(\alpha-\xi)b_\mathrm{J}/\left[\Delta\left(1+\xi^2\right)\right]$. As ϕ increases, the velocity decreases.

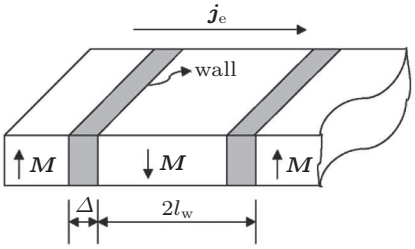


Fig. 1. Geometry of the film with stripe-domain structures. The easy axis is perpendicular to the film plane and defined as the z direction. The current is applied along the film and perpendicular to the domain wall, and Δ is the thickness of domain wall.[39]

Next, we discuss the case of small deviations of ϕ from equilibrium, and the linear variation of the wall velocity with ϕ. Linearizing Eq. (5) and eliminating ϕ using Eq. (6), we obtain

$$\begin{aligned} &m\frac{\partial^2 L}{\partial t^2} + b\frac{\partial L}{\partial t} + kL \\ &= -\frac{2M_\mathrm{s}}{\gamma(1+\xi^2)}\left(\frac{\xi}{\Delta}b_\mathrm{J} + \frac{1+\xi\alpha}{4\pi\gamma\Delta M_\mathrm{s}}\frac{\partial b_\mathrm{J}}{\partial t}\right), \end{aligned} \tag{7}$$

where $k = 16\pi M_s^2/l_W$, $\Delta = \sqrt{A/K}$, $m = \left(1+\alpha^2\right)/\left(2\pi\gamma^2\Delta\right)$, and $b = \alpha\left(2M_s/(\gamma\Delta) + k/(4\pi\gamma M_s)\right)$. In direct current case, adiabatic torque only twists the magnetization of wall, or transfers magnetic momentum to the wall, while non-adiabatic torque produces a global pressure on the wall.[12,14,45] However, in the alternating current case, equation (7) indicates that both the adiabatic torque and non-adiabatic one contribute to the global motion of wall.

For an applied direct current, equation (7) describes damped oscillation of the wall. It is easy to see that only non-adiabatic spin torque affects wall motion in the direct current case. This is because the domain wall is deemed as a particle and only non-adiabatic torque produces a pressure on it. The current changes the equilibrium location of the oscillation. In the absent of driving field, the change is evaluated as $\Delta L_0 = j_e \xi P \mu_B l_W/[8\pi e\gamma\Delta M_s^2(1+\xi^2)]$. If $\Delta L_0 \geq l_W$ (the range of the restoring potential), the wall is depinned. Consequently, the current density for depinning is

$$j_{dc}^{cri} = 8\pi(1+\xi^2)e\gamma\Delta M_s^2/(\xi P\mu_B). \tag{8}$$

For the case of alternating current, taking $j_e = j_{ac}\cos\omega t$ with oscillating frequency ω, equation (7) describes forced damped oscillations. Considering $b^2 < 4mk$, we obtain

$$\begin{aligned} L = {} & L_0 \exp\left(-\frac{bt}{2m}\right)\cos\left(\frac{\sqrt{4mk-b^2}}{2m}t\right) \\ & - \frac{2P\mu_B/\gamma e\left(1+\xi^2\right)\sqrt{\xi^2/\Delta^2+(1+\alpha\xi/4\pi\gamma M_s)^2\omega^2}\, j_{ac}}{\sqrt{\left(k-m\omega^2\right)^2+b^2\omega^2}} \\ & \times \cos\left(\omega t - \delta - \delta'\right), \end{aligned} \tag{9}$$

where

$$\begin{aligned} \delta &= \arctan\left[b\omega/\left(k^2-m\omega^2\right)\right], \\ \delta' &= \arctan\left[\left(1+\alpha\xi\right)\omega/\left(\left(1+\xi^2\right)4\pi\gamma\xi M_s\right)\right], \end{aligned}$$

and L_0 is a real constant which can be determined from the initial conditions. The first term in Eq. (9) rapidly approaches zero because of the large value of $b/2m$. From Eq. (9), the resonance frequency is $\omega = 4\pi\gamma M_s[(4\Delta^2/l_W^2+\xi^2+\xi^4)^{1/2} - \xi^2]^{1/2}$, and smaller current leads to a larger displacement. Taking $L_{max} = l_W$, we can obtain the critical alternating current density that can depin domain wall in the presence of resonance, which is

$$\begin{aligned} j_{ac}^{cri} = {} & \frac{\xi}{2}\left\{\frac{l_W}{\Delta}\left[2\sqrt{\pi}\sqrt{\left(\pi\xi^4-\alpha^2\xi^2\right)\frac{l_W^2}{\Delta^2}+4\xi^2\frac{l_W}{\Delta}+4}\right.\right. \\ & \left.\left. + \left(\alpha^2-2\pi\xi^2\right)\frac{l_W}{\Delta}-4\right]\right\}^{1/2} j_{dc}^{cri}. \end{aligned} \tag{10}$$

Using the material parameters of Co_3Pt, and taking $l_W = 1\mu m$, the resonant frequency is $\omega = 12.8$ GHz and $j_{ac}^{cri} = 0.18\, j_{dc}^{cri}$. Without the currents, to counter the restoring force, the driving field is not less than $8\pi M_s$. For example, the value is 2.8 T for Co_3Pt. Combining the magnetic field and spin current, the critical current density can also be reduced. Applying a magnetic field perpendicular to the film, we add a term $2M_sH_\perp$ to the right of Eq. (7). We obtain $\widetilde{j}_{dc}^{cri} = [1 - H_\perp/(8\pi M_s)]j_{dc}^{cri}$, and $\widetilde{j}_{dc}^{cri}$ denotes the critical current density due to driving field and current.

2.2. Screw-pitch effect and velocity oscillation of domain wall

In this section, we report analytically the critical current condition for anisotropic ferromagnetic nanowire driven only by spin-transfer torque. Below the critical current, the ferromagnetic nanowire admits only the final static domain wall solution which implies that the spin-polarized current cannot drive domain wall move continuously. When the spin-polarized current exceeds the critical value, the dynamics of domain wall exhibits the novel screw-pitch effect with the periodic temporal oscillation of domain wall velocity and width. A detail theoretical analysis and numerical simulation demonstrate that this novel phenomenon arises from the natural conjunction action of Gilbert-damping and spin-transfer torque. We also observe that the spin-transfer torque plays an entirely opposite role in the above two cases. At last, our theoretical prediction can be confirmed by the numerical simulation in terms of Runge–Kutta–Munthe–Kaas (RKMK) method.[57,58]

We consider an infinitely long uniaxial anisotropic ferromagnetic nanowire, where the electronic current flows along the long length of the wire defined as the x direction which is also the easy axis of anisotropy ferromagnet. For convenience, the magnetization is assumed to be nonuniform only in the direction of current. Since the magnetization varies slowly in space, it is reasonable to take the adiabatic limit. Then the dynamics of the localized magnetization can be described by the modified Landau–Lifshitz–Gilbert equation with spin-transfer torque[11–13]

$$\frac{\partial \boldsymbol{M}}{\partial t} = -\gamma \boldsymbol{M}\times H_{eff} + \frac{\alpha}{M_s}\boldsymbol{M}\times\frac{\partial \boldsymbol{M}}{\partial t} + \boldsymbol{\tau}_b, \tag{11}$$

where $\boldsymbol{H}_{eff}$ represents the effective magnetic field. For the uniaxial ferromagnetic nanowire, the effective field can be written as $\boldsymbol{H}_{eff} = \left(2A/M_s^2\right)\left(\partial^2\boldsymbol{M}/\partial x^2\right) + H_xM_x/M_s\boldsymbol{e}_x - 4\pi M_z\boldsymbol{e}_z$, where A is the exchange constant, H_x is the anisotropy field, and $\boldsymbol{e}_i$ $(i = x, y, z)$ is the unit vector, respectively. Introducing the normalized magnetization, i.e., $\boldsymbol{m} = M/M_s$, equation (11) can be simplified into the dimensionless form

$$\begin{aligned} \alpha_1\frac{\partial \boldsymbol{m}}{\partial t} = {} & -\boldsymbol{m}\times h_{eff} - \alpha\boldsymbol{m}\times(\boldsymbol{m}\times h_{eff}) \\ & + \alpha b_1\boldsymbol{m}\times\frac{\partial \boldsymbol{m}}{\partial x} + b_1\frac{\partial \boldsymbol{m}}{\partial x}, \end{aligned} \tag{12}$$

where $\alpha_1 = (1+\alpha^2)$ and $b_1 = b_J t_0/l_0$. Here b_J is given in advance. In this section, the time t and space coordinate x have been rescaled by the characteristic time $t_0 = 1/(16\pi\gamma M_s)$ and length $l_0 = \sqrt{A/(8\pi M_s^2)}$, respectively. The dimensionless effective field becomes $\boldsymbol{h}_{\rm eff} = \partial^2\boldsymbol{m}/\partial x^2 + C_x m_x \boldsymbol{e}_x - C_z m_z \boldsymbol{e}_z$, with $C_x = H_x/(16\pi M_s)$ and $C_z = 0.25$.

In the following, we seek for the exact domain wall solutions of Eq. (12), and then study the dynamics of magnetization driven by spin-transfer torque. For this purpose, we make the ansatz

$$m_x = \tanh\Theta_D, m_y = \frac{\sin\phi_D}{\cosh\Theta_D}, m_z = \frac{\cos\phi_D}{\cosh\Theta_D}, \tag{13}$$

where $\Theta_D = k_1 x - \omega_1 t$, and the time- and space-independent parameters ϕ_D, k_1, and ω_1 are to be determined, respectively. Substituting Eq. (13) into Eq. (12), we have

$$k_1^2 = C_x + C_z\cos^2\phi_D, \tag{14}$$

$$-\omega_1(1+\alpha^2) = b_1 k_1 + C_z\sin\phi_D\cos\phi_D, \tag{15}$$

$$\alpha b_1 k_1\cos\phi_D = \alpha(C_x - k_1^2)\sin\phi_D, \tag{16}$$

$$\alpha b_1 k_1\sin\phi_D = -\alpha C_z\sin^2\phi_D\cos\phi_D. \tag{17}$$

From the above equations we can obtain three cases of domain wall solutions for Eq. (12). Firstly, in the absence of damping, equations (14)–(17)) admit the solution

$$k_1 = \pm\sqrt{C_x + C_z\cos^2\phi_D}, \omega_1 = -b_1 k_1 - \frac{C_z}{2}\sin(2\phi_D), \tag{18}$$

where ϕ_D is the arbitrary angle. This solution shows that the spin-transfer torque contributes a dimensionless velocity $-b_1$ only without damping. The velocity of domain wall is formed by two parts, i.e., $v = -(C_z\sin 2\phi_D)/(2k_1) - b_1$, which can be affected by adjusting the angle ϕ_D and the spin-transfer torque. Secondly, in the absence of spin torque, we have the solution of Eqs. (14)–(17) as $\omega_1 = 0$, $\phi_D = \pm\pi/2$, and $k_1 = \pm\sqrt{C_x}$, i.e., the static domain wall solution. In terms of RKMK method,[57,58] we perform direct numerical simulation for Eq. (12) with various initial conditions, and all numerical results show that the damping drives the change of ϕ_D, which in turn affects the domain wall velocity and width defined by $1/|k_1|$. At last, $\phi_D = \pm\pi/2, \omega_1 = 0$, i.e., the domain wall stops completely, and the domain wall width achieves its maximum value $\sqrt{C_x}$, which confirms Walker's analysis[16] that the damping prevents domain wall from moving without the external magnetic field or spin-transfer torque. However, as shown later, the presence of damping is prerequisite for the novel screw-pitch property of domain wall driven by spin-transfer torque. At last, we consider the case of the presence of damping and spin-transfer torque. Solving Eqs. (14)–(17), we have

$$k_1 = \pm\frac{1}{2}(B_1 - \sqrt{B_2}), \quad \omega_1 = 0, \quad \sin 2\phi_D = -\frac{2b_1 k_1}{C_z}, \tag{19}$$

where $B_1 = 2C_x + C_z - b_1^2$, and $B_2 = (C_z - b_1^2)^2 - 4C_x b_1^2$.

It is clear that equation (19) implies the critical spin-polarized current condition, namely,

$$b_J \le (\sqrt{C_x + C_z} - \sqrt{C_x}) l_0/t_0,$$

which is determined by the character velocity l_0/t_0, the anisotropic parameter C_x, and the demagnetization parameter C_z. Below the critical current, i.e., $b_1^2 \le (\sqrt{C_x + C_z} - \sqrt{C_x})^2$, the domain wall width falls into the range of $1/\sqrt{C_x + C_x C_z} \le 1/|k_1| \le 1/C_x$. From Eq. (19), we obtain four solutions of ϕ_D, i.e., $\phi_D = \pm\pi/2 + 1/2\arcsin(2b_1 k_1/C_z)$ for $k_1 > 0$ and $\phi_D = \pm\pi/2 - 1/2\arcsin(2b_1|k_1|/C_z)$ for $k_1 < 0$. In fact, the signs "+" and "−" in Eq. (19) denote kink and anti-kink solution, respectively, and the corresponding solution in Eq. (13) represents the static tail-to-tail or head-to-head Néel domain wall, respectively. This result shows that below the critical current, the final equilibrium domain wall solution must be realized by the condition that $\boldsymbol{m}\times h_{\rm eff} = b_1\partial\boldsymbol{m}/\partial x$. It clearly demonstrates that the spin-transfer torque has two interesting effects. One is that the term $b_1\partial\boldsymbol{m}/\partial x$ in Eq. (12) plays the anti-precession role counteracting the precession driven by the effective field $\boldsymbol{h}_{\rm eff}$. However, the third term in the right hand of Eq. (13), namely, $\alpha b_1\boldsymbol{m}\times(\partial\boldsymbol{m}/\partial x)$, has the anti-damping effect counteracting the damping term $-\alpha\boldsymbol{m}\times(\boldsymbol{m}\times h_{\rm eff})$. It is to say that below the critical value, the spin-polarized current cannot drive domain wall move continuously without the applied external magnetic field.

When the spin-polarized current exceeds the critical value, the dynamics of domain wall exhibits two novel properties, as will be shown in the following section. Above the critical current, the precession term $-\boldsymbol{m}\times h_{\rm eff}$ cannot be counteracted by spin-transfer torque, and the static domain wall solution of Eq. (12) does not exist. Because the magnetization magnitude is constant, i.e., $\boldsymbol{m}^2 = 1$, so we have $\boldsymbol{m}\cdot(\partial\boldsymbol{m}/\partial x) = 0$, which shows that the direction of $\partial\boldsymbol{m}/\partial x$ is always perpendicular to the direction of $\boldsymbol{m}$, or $\partial\boldsymbol{m}/\partial x = 0$. It is well known that a magnetic domain wall separates two opposite domains by minimizing the energy. In the magnetic domain wall, the direction of magnetic moments gradually changes, i.e., $\partial\boldsymbol{m}/\partial x \neq 0$, so the direction of $\partial\boldsymbol{m}/\partial x$ should adopt the former case. Out of region of domain wall, the normalized magnetization will site at the easy axis, i.e., $m_x = 1$ (or -1), in which $\partial\boldsymbol{m}/\partial x = 0$.

Under the above consideration, we make a detail analysis of Eq. (12). As a characteristic view, we mainly consider the domain wall center, defined by $m_x = 0$. The magnetic moment must be in the y–z plane, while the direction of $\partial\boldsymbol{m}/\partial x$ should lay in the x axis ($+x$ axis for $k_1 > 0$, and $-x$ axis for $k_1 < 0$). In order to satisfy Eq. (12), the magnetic moment in domain wall center should include both the precession around the effective spin-torque field $\alpha b_1\partial\boldsymbol{m}/\partial x$ and the tendency along the direction of $\partial\boldsymbol{m}/\partial x$ continuously from the last two terms

on the right-hand side of Eq. (12). The former precession motion implies that the parameter $\phi_{\rm D}$ will rotate around the x axis continuously, while the latter tendency forces the domain wall center to move toward the opposite direction of the current, i.e., the $-x$-axis direction, confirming the experiment[40–44] in magnetic thin films and magnetic wires. Combining the above two effects, we find that this rotating and moving phenomenon is very similar to screw-pitch effect. The continuous rotation of magnetic moment in domain wall center, i.e., the periodic change of $\phi_{\rm D}$, can result in the periodic oscillation of domain wall velocity and width from Eq. (18) under the action of the first two terms on the right-hand side of Eq. (12). It is interesting to emphasize that when the current exceeds the critical value, the term $\alpha b_1 \boldsymbol{m} \times (\partial \boldsymbol{m}/\partial x)$ plays the role of inducing the precession, while the term $b_1 \partial \boldsymbol{m}/\partial x$ has the effect of damping, which is even entirely contrary to the case where the current is below the critical value as mentioned above. From the above discussion we conclude that the motion of magnetic moment in the domain wall center will not stop, except it falls into the easy axis, i.e., out of the range of domain wall. In fact, all the magnetic moments in domain wall can be analyzed in detail with the above similar procedure.

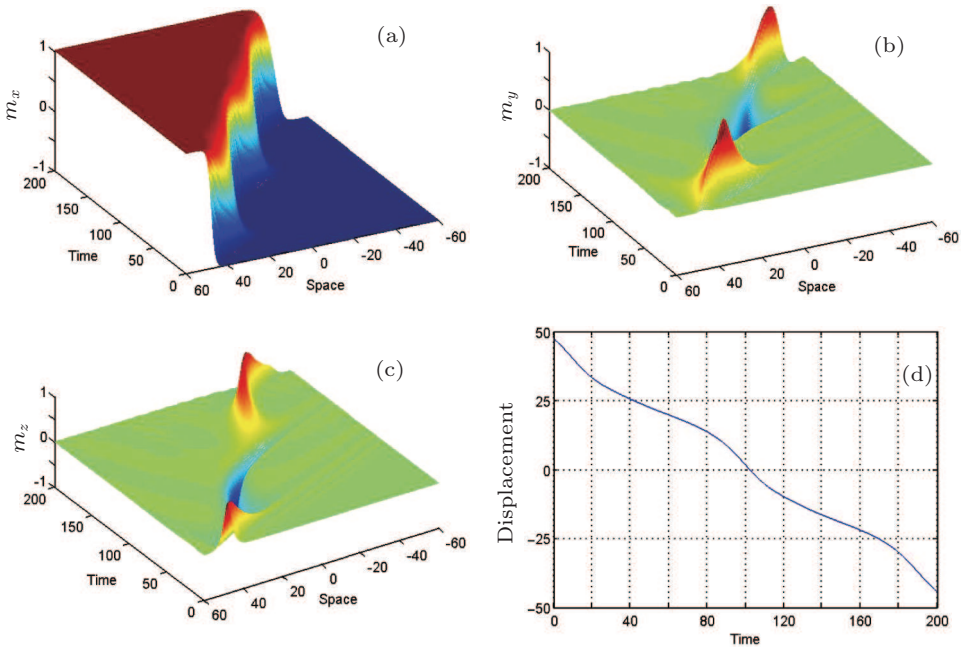


Fig. 2. Dynamics of domain wall above the critical current. (a)–(c) Evolution of the normalized magnetization $\boldsymbol{m}$. (d) Displacement of domain wall driven only by spin-transfer torque. The parameters are $\alpha = 0.2$, $C_x = 0.05$, $C_z = 0.25$, $b_{\rm J} = 0.6$, and the initial angle $\phi = 0.01\pi$.[59]

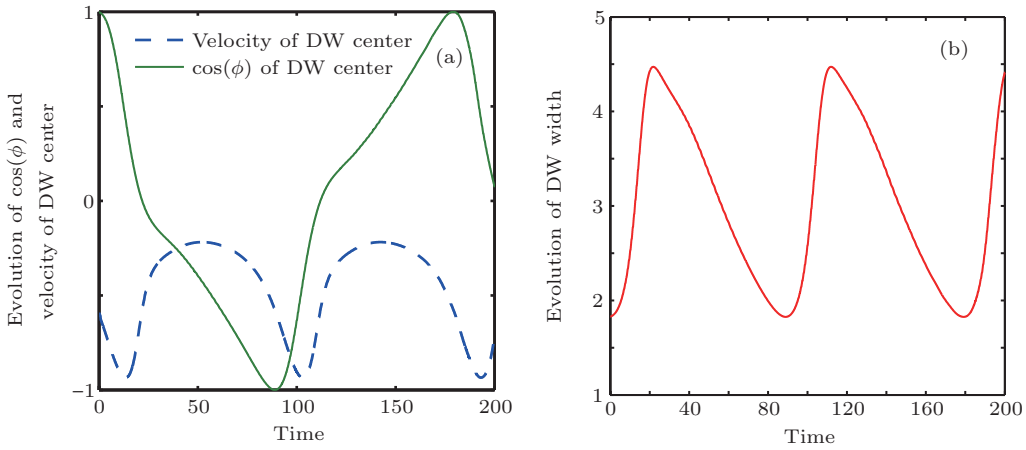


Fig. 3. (a) Evolution of $\cos\phi$ and periodic oscillation of domain wall (DW) velocity. (b) Periodic temporal oscillation of domain wall width. The parameters are the same as those in Fig. 2.[59]

Now it is clear for the dynamics of domain wall driven only by spin-transfer torque. Coming back to Eq. (12), we can see that this novel screw-pitch effect with the periodic oscillation of domain wall velocity and width occurs even at the conjunct action of the damping and spin-transfer torque. To confirm our theoretical prediction, we perform direct numer-

ical simulation for Eq. (12) with an arbitrary initial condition by means of the RKMK method[57,58] with the current exceeding the critical value. In Figs. 2(a)–2(c) we plot the time evolution of the normalized magnetization $\boldsymbol{m}$, while the displacement of domain wall center is shown in Fig. 2(d). The result in Fig. 2 entirely confirms our theoretical analysis above. The evolution of $\cos\phi_{\mathrm{D}}$ and the domain wall velocity and width are shown in Fig. 3. From Fig. 3 we can see that the periodic change of $\cos\phi_{\mathrm{D}}$ leads to the periodic temporal oscillation of domain wall velocity and width. From Eq. (18) and the third term of Eq. (12) we can infer that $\cos\phi_{\mathrm{D}}$ undergoes uneven change as shown in Fig. 3(a), i.e., the time corresponding to $0 < \phi_{\mathrm{D}} + n\pi \leq \pi/2$ is shorter than that corresponding to $\pi/2 < \phi_{\mathrm{D}} + n\pi \leq \pi$ $(n = 1, 2, \ldots)$ in each period, and the domain wall velocity has the same character. This causes the domain wall displacement to increase rapidly at first and then slowly, as shown in Fig. 2(d). This phenomenon clarifies clearly the presence of screw-pitch effect. The domain wall velocity oscillation driven by the external magnetic field has been observed experimentally.[19] Our theoretical prediction for the range of domain wall velocity oscillation driven by the above critical current could be observed experimentally.

2.3. Nonautonomous helical motion of magnetization in ferromagnetic nanowire

A domain wall can propagate under a spin-polarized current through angular-momentum transfer from conduction electrons to the local magnetization, known as the spin-transfer torque. Recently, another interesting issue regarding the spin-transfer torque effect in some conditions could destabilize the reference layer and cause its propagation. From the pioneering theory of spin-transfer torque, Slonczewski has pointed out that large current maybe drive the pinwheel motion of the magnetization in the two magnetic layers for the instability of the reference layer. Some experiments have demonstrated that the spin torque could rotate the magnetization of the reference layer and trigger the radio frequency oscillations and intense microwave emission peaks.

In this section, we focus on an infinite biaxial anisotropic ferromagnetic nanowire. The easy axis is along the wire defined as the z direction, and the hard axis is perpendicular to the wire axis, as shown in Fig. 4. The localized magnetization $\boldsymbol{M}(z,t)$ with the saturation magnetization M_{s} is assumed nonuniform only in the z direction. As a model system, we assume that the reference layer has been partially fixed, due to the current Joule heating effect, the magnetization direction could be rotated at current density high enough. The magnetizations of the free and reference layers interact with each other via the spin-transfer torque effect and each layer serves as a polarizer for the other one. In order to separate the contribution of the torque effect to the reference layer rotation from other possible reasons, here only the traditional formula of spin-torque effect is taken into account in our model.

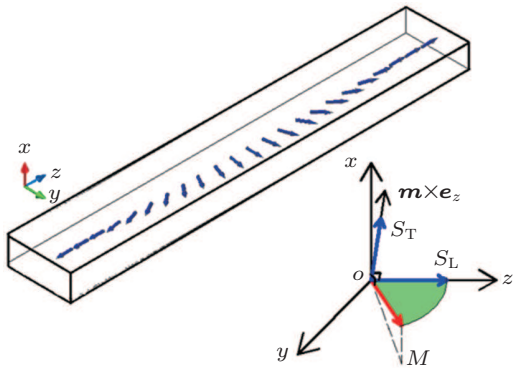


Fig. 4. Schematic drawing of the ferromagnetic nanowire and the coordinate system. The easy axis is perpendicular to the nanowire and defined as the z direction. S_{L} and S_{T} represent the constant longitudinal density along the z axis and the temporal and spatial dependent transverse density.[53]

Thus, we can adopt Slonczewski torque[8] $\boldsymbol{T}_{\mathrm{STT}}$ which generally takes the form of $\boldsymbol{T}_{\mathrm{STT}} = \gamma \boldsymbol{m} \times (\boldsymbol{m} \times \boldsymbol{S})$, where γ is the gyromagnetic ratio, $\boldsymbol{m}$ is the normalized magnetization, i.e., $\boldsymbol{m}(z,t) = \boldsymbol{M}(z,t)/M_{\mathrm{s}}$, and $\boldsymbol{S} = S_{\mathrm{L}}\boldsymbol{e}_z + S_{\mathrm{T}}(z,t)\,\boldsymbol{m} \times \boldsymbol{e}_z$ with $S_{\mathrm{L,T}} = j_{\mathrm{L,T}} P\hbar/(2\mathrm{d}\,|e|)$, where the subscript L and T represent the constant longitudinal density along the z axis and the temporal and spatial dependent transverse density which arises from partially fixed reference layer and can induce the free layer procession, respectively. The parameter d is the thickness of the free magnetic layer, and e is the magnitude of electron charge.

Driven by the spin-polarized current with temporal dependence, the nonautonomous dynamics of magnetic domain wall can be described by the modified Landau–Lifshitz–Gilbert equation with spin-transfer torque[5,8,10]

$$\frac{\partial \boldsymbol{M}}{\partial t} = -\gamma \boldsymbol{M} \times \boldsymbol{H}_{\mathrm{eff}} + \frac{\alpha}{M_{\mathrm{s}}} \boldsymbol{M} \times \frac{\partial \boldsymbol{M}}{\partial t} + \boldsymbol{T}_{\mathrm{STT}}, \tag{20}$$

where the effective field takes the form of $\boldsymbol{H}_{\mathrm{eff}} = [K_x M_x \boldsymbol{e}_x - K_z M_z \boldsymbol{e}_z - A(\partial_z^2 \boldsymbol{M})]/(\mu_0 M_{\mathrm{s}}^2) + \boldsymbol{H}_{\mathrm{ext}}$. Here K_x and K_z denote the energetic anisotropy constant along the hard and easy axis, respectively. The parameter A is the exchange interaction coefficient, and $\boldsymbol{e}_i$ $(i = x, y, z)$ is the unit vector, respectively. In this subsection, we consider the external magnetic field $\boldsymbol{H}_{\mathrm{ext}}$ with temporal and spatial dependence and equation (20) reduces to the dimensionless form

$$\frac{1}{\Gamma}\frac{\partial \boldsymbol{m}}{\partial t} = -\boldsymbol{m} \times [\boldsymbol{h}_{\mathrm{eff}} - \alpha \boldsymbol{s} + \boldsymbol{m} \times (\alpha \boldsymbol{h}_{\mathrm{eff}} + \boldsymbol{s})], \tag{21}$$

where $\Gamma = 1/(1+\alpha^2)$, the dimensionless effective field $\boldsymbol{h}_{\mathrm{eff}} = \partial_z^2 \boldsymbol{m} - k_x m_x \boldsymbol{e}_x + k_z m_z \boldsymbol{e}_z + \boldsymbol{h}_{\mathrm{ext}}$ with $k_{x,z} \equiv K_{x,z}/(\mu_0 M_{\mathrm{s}})$, $\boldsymbol{h}_{\mathrm{ext}} = \boldsymbol{H}_{\mathrm{ext}}/M_{\mathrm{s}} \equiv -h_{\mathrm{L}}\boldsymbol{e}_z - h_{\mathrm{T}}\boldsymbol{m} \times \boldsymbol{e}_z$, and the dimensionless spin torque $\boldsymbol{s} \equiv S/M_{\mathrm{s}}$. In Eq. (21) we have rescaled the time t and space coordinate x by the characteristic time $1/(\gamma M_{\mathrm{s}})$ and length $\sqrt{A/(\mu_0 M_{\mathrm{s}}^2)}$, respectively.

In terms of the spherical coordinate, i.e., $\boldsymbol{m} = (\sin\theta\cos\phi, \sin\theta\sin\phi, \cos\theta)$, equation (21) becomes

$$\frac{\partial\phi}{\partial t}\sin\theta - \alpha\frac{\partial\theta}{\partial t} = \frac{1}{2}\left(k_x\cos^2\phi + k_z\right)\sin 2\theta - \frac{\partial^2\theta}{\partial z^2} - (h_{\rm L} - S_{\rm T})\sin\theta, \tag{22}$$

$$\alpha\frac{\partial\phi}{\partial t}\sin\theta + \frac{\partial\theta}{\partial t} = (\frac{k_x}{2}\sin 2\phi + h_{\rm T} + S_{\rm L})\sin\theta. \tag{23}$$

According to Eqs. (22) and (23), we assume $\ln\tan(\theta/2) = (z - L(t))/W_0$ in which $L(t)$ is the domain wall center, and the constant width W_0 and the cant angle $\phi(t)$ of domain wall are to be determined. In order to force the width of the domain wall to remain constant, i.e., $W_0 = 1/\sqrt{k_x + k_z}$, and the time- and space-dependent transverse spin current should takes the form of $S_{\rm T}(z,t) = -k_x\sin^2\phi\tanh\theta$. Thus, the domain wall profile satisfies $(k_x + k_z)\sin 2\theta - 2\partial^2\theta/\partial z^2 = 0$ with boundary condition of $\theta = 0$ and π at long distance. Substituting this domain wall profile into Eqs. (22) and (23), the domain wall velocity and domain wall's rotational motion obey

$$V \equiv \frac{\partial L}{\partial t} = -\frac{W_0}{\alpha}\left(h_{\rm L} + \frac{\partial\phi}{\partial t}\right), \tag{24}$$

$$\frac{\partial\phi}{\partial t} = \Gamma C + \Gamma C_{\rm m}\sin(2\phi), \tag{25}$$

where the parameters are defined by $C_{\rm m} = \alpha k_x/2$ and $C = \alpha(S_{\rm L} + h_{\rm T}) - h_{\rm L}$.

Equations (24) and (25) present the novel motion of nonautonomous domain wall and constitute our main results in this paper. Equation (24) shows that the domain wall velocity is composed of two parts: the longitudinal external field $h_{\rm L}$ along the easy axis and the coherent domain wall rotation velocity $\partial\phi/\partial t$, which may result in the periodic oscillation of domain wall velocity. The domain wall velocity is also affected by the damping parameter α and the domain wall width W_0 determined by the energetic anisotropy constants. As shown in Eq. (25), the domain wall rotates coherently under the action of the time- and space-dependent current and field. It is characterized by the constant velocity ΓC arising from the external driving force and the temporal periodic velocity with the amplitude $\Gamma C_{\rm m}$ determined by the internal transverse anisotropy parameter k_x. Integrating Eqs. (24) and (25), the domain wall displacement admits

$$L(t) = -\frac{W_0}{\alpha}[h_{\rm L}t + \Gamma\int_0^t (C + C_{\rm m}\sin(2\phi))\,{\rm d}t]. \tag{26}$$

According to the above analysis, we can call this rotating and moving magnetization in domain wall depicted by Eqs. (24) and (25) as the nonautonomous helical motion or screw-pitch effect.[59]

By tuning the longitudinal value $S_{\rm L}$ for the spin-polarized current and the external field $\boldsymbol{h}_{\rm ext}$, the coherent domain wall rotation exhibits different feature, which in turn affects the domain wall velocity and dispiration. For different relations of C and $C_{\rm m}$, equation (25) can admit the three cases of solution. For convenience, in the following discussion we assume that $h_{\rm T,L}$ and $S_{\rm L}$ are constant, respectively. Firstly, we assume that the applied current and external field are small, i.e., $C < C_{\rm m}$. Integrating Eq. (25) we have

$$\sin(2\phi) = -\frac{CB^2 - 2C_{\rm m}B + C}{C_{\rm m}B^2 - 2CB + C_{\rm m}}, \tag{27}$$

where $B = {\rm e}^{-2\Gamma\sqrt{\kappa_1\kappa_2}t}$ with $\kappa_1 = C_{\rm m} - C$ and $\kappa_2 = C_{\rm m} + C$. When $t \to \infty$, the domain wall stops the rotation and the cant angle attains its extremum, i.e., $\sin(2\phi) \to -C/C_{\rm m}$, which is also confirmed in Eq. (25). At the same time, the domain wall velocity in Eq. (24) takes the form $V = -W_0 h_{\rm L}/\alpha$ which can be controlled by adjusting the longitudinal external field $h_{\rm L}$. In this case, the domain wall displacement $L(t)$ in Eq. (26) takes the form

$$L(t) = -\frac{W_0}{\alpha}\left(h_{\rm L}t + \arctan\sqrt{\frac{\kappa_1}{\kappa_2}} - \arctan\frac{\zeta(t)}{\sqrt{\kappa_1\kappa_2}}\right),$$

where $\zeta(t) = C_{\rm m}B - C$. Secondly, when the internal transverse anisotropy parameter k_x is balanced by the applied current and external field, i.e., $C = C_{\rm m}$, equation (25) admits the solution

$$\sin(2\phi) = \frac{1 - (2\Gamma C t)^2}{1 + (2\Gamma C t)^2}, \tag{28}$$

which also implies that the domain wall stops the rotation in the limit $t \to \infty$, and the cant angle reads $\sin(2\phi) \to -1$. Then the domain wall velocity has the same results as the above case, while the domain wall displacement becomes $L(t) = -W_0/\alpha[h_{\rm L}t + \arctan(2\Gamma C t)]$.

Based on the above results for $C \le C_{\rm m}$, we find that there is a critical value for current and/or field. In the absence of external filed, this critical condition takes the special form $S_{\rm Lc} = k_x/2$. Below this critical current, the domain wall finally stops the coherent rotation, resulting in the static domain wall solution with the arbitrary initial domain wall state. In both cases, the domain wall velocity is controlled finally by the longitudinal external filed $h_{\rm L}$ which is enhanced by the damping factor α. The graphic illustration for the cases $C \le C_{\rm m}$ for domain wall rotation velocity, domain wall velocity, and displacement is shown in Fig. 5. Comparing two cases of $C < C_{\rm m}$ and $C = C_{\rm m}$ in Fig. 5, it can be found that the domain wall rotation velocity increases with increasing C initially. Finally, the domain wall stops rotation and the domain wall velocity and displacement are proportional to the longitudinal filed value $h_{\rm L}$, which is also confirmed in Eqs. (24)–(26).

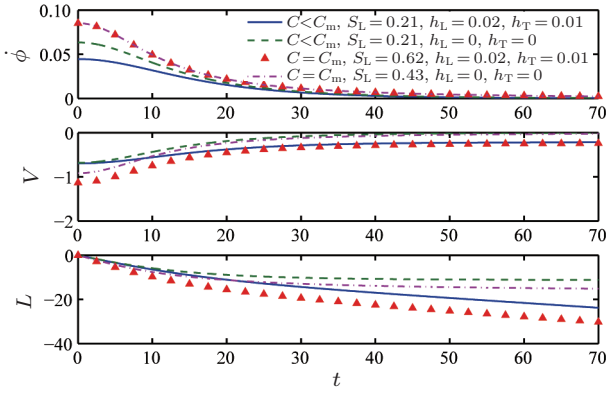


Fig. 5. Graphic illustration of domain wall rotation velocity ($\dot{\phi} = \partial\phi/\partial t$), domain wall velocity, and displacement in the cases $C \leq C_m$. The parameters are $\alpha = 0.1$, $k_x = 0.86$, and $k_z = 5 \times 10^{-4}$.[53]

When the applied current and external field are increased beyond this critical value, i.e., $C > C_m$, the domain wall always rotates with the easy axis with velocity $\partial\phi/\partial t$ and possesses the nonautonomous helical motion. Integrating Eq. (25) we obtain the solution

$$\sin(2\phi) = -\frac{\kappa_2 + \kappa_1 \tan^2(\omega t)}{\kappa_2 - \kappa_1 \tan^2(\omega t)}, \tag{29}$$

where $\omega = \Gamma\sqrt{-\kappa_1\kappa_2}$. When $t = n\pi/(2\omega)$ $(n = 0, 1, \ldots)$, equation (29) gets its extremum, i.e., $|\sin(2\phi)| = 1$. From Eqs. (25) and (29), we see that the domain wall rotates coherently with the constant velocity ΓC and the temporal periodic velocity with the amplitude C_m and frequency ω. The former is controlled by the longitudinal spin-polarized current S_L and the external field $h_{T,L}$, while the latter is related to the internal transverse anisotropy parameter k_x. Even in the absence of external filed, this interesting phenomenon can occur and the domain wall velocity and rotation is controlled only by the longitudinal spin-polarized current S_L obtained from Eq. (24). The domain wall rotation becomes more rapid with increasing parameter C, which can be realized by adjusting the external driving force.

With the expressions of C and C_m, we can rewrite the domain wall velocity in Eq. (24) as

$$V = -W_0\Gamma\left(\alpha h_L + S_L + h_T + \frac{1}{2}k_x \sin(2\phi)\right), \tag{30}$$

which implies that the longitudinal spin-polarized current S_L and the transversal external field h_T contribute to the fast domain wall velocity, while the longitudinal external field h_L is weakened by the damping factor α. Compared with the case of $C \leq C_m$, the domain wall velocity becomes slow with the same the longitudinal external field h_L. With this rotating motion of magnetization, the domain wall displacement in Eq. (26) is composed of the linear and the nonlinear contribution. The result in Eq. (26) also demonstrates that the domain wall moves through the same displacement for each time period, i.e., $T_0 = \pi/\omega$.

In Figs. 6 and 7, we illustrate the properties of the nonautonomous domain wall motion for two cases where C is slightly above the critical value and $C \gg C_m$. Figure 6 indicates that the domain wall rotates periodically and exhibits a nonuniform velocity in each period. It rotates slowly at first, and finally rapidly in the middle of each period. The domain wall velocity and displacement in turn takes the same vision. For $C \gg C_m$ (see Fig. 7), the domain wall possesses the sinusoidal oscillation nearly for domain wall rotation and velocity, while the domain wall displacement takes the linear response to time which is also confirmed by the special form $L(t) = -tW_0(\omega + h_L)/\alpha$ obtained from Eq. (26) with $\kappa_1 \sim \kappa_2$. In order to analyze the relationship between C and C_m deeply, we can consider the motion of domain wall in the limit $t \to \infty$. It is obvious that the critical point is formed by $C = C_m$. As shown in Fig. 8(a), for $C \leqslant C_m$, the domain wall will stop and the rotation velocity is also confirmed by $\partial\phi/\partial t\,(\infty) = 0$ in Eq. (25). At the same time, the domain wall velocity in Eq. (24) takes the form $V(\infty) = -W_0 h_L/\alpha$, which can be controlled by adjusting the longitudinal external field h_L. Because the domain wall motion is temporally periodic for $C > C_m$, we can define the average rotation velocity $\partial\phi/\partial t\,(\infty) \equiv \overline{\partial\phi/\partial t}$ and $V(\infty) \equiv \overline{V}$ for each time period π/ω, when $t \to \infty$.

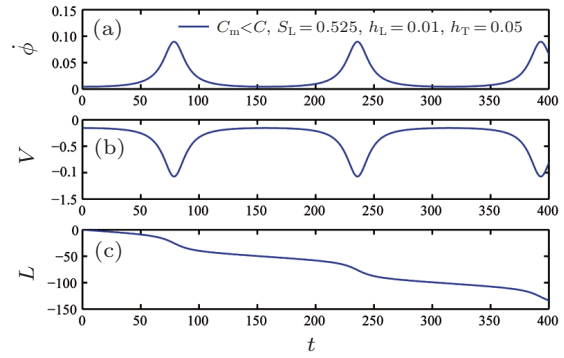


Fig. 6. Nonautonomous domain wall motion in the case of $C > C_m$, namely, C is slightly greater than the critical value. (a) Domain wall rotation velocity ($\dot{\phi} = \partial\phi/\partial t$), (b) domain wall velocity, and (c) domain wall displacement. Other parameters are the same as those in Fig. 5.[53]

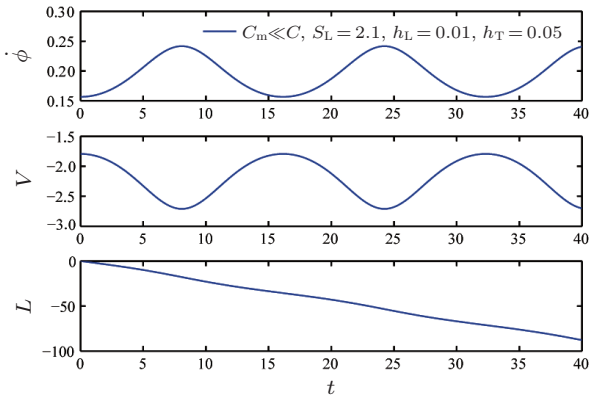


Fig. 7. Nonautonomous motion of domain wall rotation velocity ($\dot{\phi} = \partial\phi/\partial t$), domain wall velocity, and displacement in the case of $C \gg C_m$. Other parameters are the same as those in Fig. 5.[53]

As the parameter C increases, $\partial\phi/\partial t\,(\infty)$ and $V\,(\infty)$ will also be linear in Fig. 8(b).

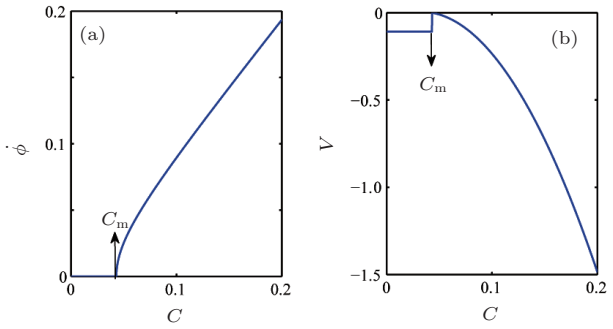


Fig. 8. Graphic illustration of (a) domain wall rotation velocity ($\dot{\phi} = \partial\phi/\partial t$) and (b) domain wall velocity for different C. The parameter S_L ranges form 0 to 2. Other parameters are $\alpha = 0.1$, $k_1 = 0.86$, $k_2 = 5\times10^{-4}$, $h_L = 0.01$, and $h_T = 0.1$.[53]

The above analysis shows that the nonautonomous domain wall solution brings forth the complicated interesting motion under the action of different external field and spin-polarized current with the spatial dependence. In order to clarify this scheme clearly, we project the expression of $\boldsymbol{h}_{\rm ext}$ and $\boldsymbol{s}$ into a special normal coordinate system, namely, $(\boldsymbol{m}, \partial\hat{m}/\partial z, \boldsymbol{m}\times\partial\hat{m}/\partial z)$, where $\partial\hat{m}/\partial z \equiv (\partial\boldsymbol{m}/\partial z)/|\partial\boldsymbol{m}/\partial z|$, as shown in Fig. 9(a). Furthermore, figure 9(b) is a plan view which clearly illustrates that the external magnetic field and spin polarization of current fall into the plane of $(\partial\hat{m}/\partial z, \boldsymbol{m}\times\partial\hat{m}/\partial z)$ to the moment. From Eq. (21), it is obvious to conclude that only the applied field and spin polarization of current falling into the plane of $(\partial\hat{m}/\partial z, \boldsymbol{m}\times\partial\hat{m}/\partial z)$ can contribute to the dynamics of local magnetization. It also clarifies that the longitudinal part S_L of current in fact results in the adiabatic spin-transfer torque and the spatial dependence part $S_T(z,t)$ play the same role of nonadiabatic spin-transfer torque, while may be realized by the partially fixed magnetization in the reference layer.

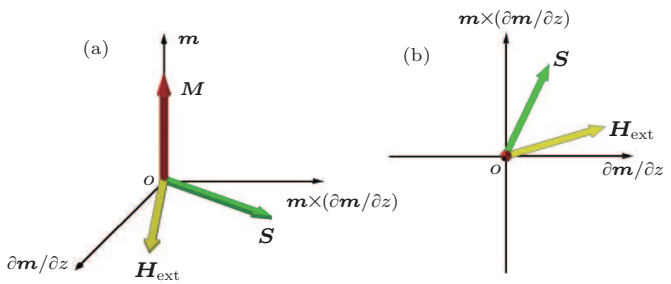


Fig. 9. Schematic of a special normal coordinate system, namely, $(\boldsymbol{m}, \partial\hat{m}/\partial z, \boldsymbol{m}\times\partial\hat{m}/\partial z)$, where $\partial\hat{m}/\partial z \equiv (\partial\boldsymbol{m}/\partial z)/|\partial\boldsymbol{m}/\partial z|$. The external magnetic field $\boldsymbol{H}_{\rm ext}$ and the polarization of current $\boldsymbol{S}$ fall into the plane of $(\partial\hat{m}/\partial z, \boldsymbol{m}\times\partial\hat{m}/\partial z)$. (a) Three-dimensional diagram and (b) a plan view.[53]

3. Current driven dynamics of soliton

We consider a very long ferromagnetic nanowire with uniform cross section, as shown in Fig. 10. For excellent approximation, this nanowire can be viewed as infinite in length. The electronic current flows along the long length of the wire, defined as the x direction. The z axis is taken as the directions of uniaxial anisotropy field and external field. Also, we assume that the magnetization is nonuniform only in the direction of current. The current injected in the nanowire can be polarized and produces a spin torque acting on the local magnetization. Thus, the modified Landau–Lifshitz–Gilbert equation with this spin torque is

$$\frac{\partial\boldsymbol{M}}{\partial t} = -\gamma\boldsymbol{M}\times\boldsymbol{H}_{\rm eff} + \frac{\alpha}{M_s}\boldsymbol{M}\times\frac{\partial\boldsymbol{M}}{\partial t} + \boldsymbol{\tau}_b, \tag{31}$$

where $\boldsymbol{H}_{\rm eff}$ is the effective magnetic field. This effective field can be written as

$$\boldsymbol{H}_{\rm eff} = \left(2A/M_s^2\right)\partial^2\boldsymbol{M}/\partial x^2 + \left[(H_K/M_s - 4\pi)M_z + H_{\rm ext}\right]\boldsymbol{e}_z,$$

where A is the exchange constant, H_K is the anisotropy field, $H_{\rm ext}$ is the applied field, and $\boldsymbol{e}_z$ is the unit vector along the z direction.

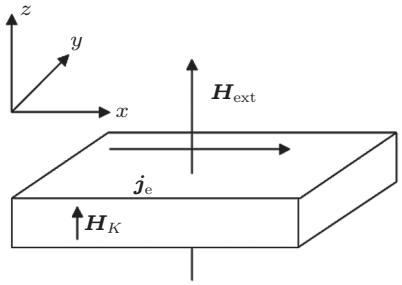


Fig. 10. Geometry of the ferromagnetic nanowire. The magnetic anisotropy field H_K and the applied magnetic field $H_{\rm ext}$ are along the vertical direction of film (the z axis). The applied current $\boldsymbol{j}_e$ flows along the nanowire (the x axis).[38]

In the following, we will discuss the linear and nonlinear magnetization dynamics in a uniaxial ferromagnetic nanowire injected with current. By stereographic projection of the unit sphere of magnetization onto a complex plane,[60] we transform the Landau–Lifshitz–Gilbert equation into a nonlinear equation of complex function and obtain two kinds of soliton solutions propagating along the wire's axis for a high-Q model and low-Q one ($Q = H_K/(4\pi M_s)$ is the quality factor). From these solutions, we study the effect of spin-polarized current on the nonlinear excitation of the magnetization in the ferromagnetic metal nanowire.

3.1. Dark soliton

When the uniaxial anisotropy field is larger than the demagnetization field, namely, $Q > 1$ (this is the case for some metallic magnetic films[61] and multilayers[62]), we can obtain dark magnetic solitons for m_z component. After rescaling the time coordinate and space coordinate by characteristic time $t_0' = 1/(\gamma(H_K - 4\pi M_s))$ and length $l_0' =$

$\sqrt{2A/((H_K-4\pi M_s)M_s)}$ and taking $\boldsymbol{M}=M_s\boldsymbol{m}$, the Landau–Lifshitz–Gilbert equation (31) can be simplified as

$$\begin{aligned}\frac{\partial \boldsymbol{m}}{\partial t} &= -(\boldsymbol{m}\times\left(\frac{\partial^2\boldsymbol{m}}{\partial x^2}\right)\\ &\quad -\left(m_z+\frac{H_{\rm ext}}{H_K-4\pi M_s}\right)(\boldsymbol{m}\times e_z)\\ &\quad +\alpha\boldsymbol{m}\times\frac{\partial\boldsymbol{m}}{\partial t}+\frac{b_{\rm J}t_0'}{l_0'}\frac{\partial\boldsymbol{m}}{\partial x}. \end{aligned}\tag{32}$$

Considering the fact that the magnitude of the magnetization is a constant at temperature well below the Curie temperature, namely, $\boldsymbol{m}^2=(\boldsymbol{M}/M_s)^2=1$, it is reasonable to take stereographic transformation,[60] $\psi=(m_x+{\rm i}m_y)/(1+m_z)$. We will obtain linear and nonlinear dynamics of magnetization from ψ.

As shown in Ref. [29], the spin wave solution of Landau–Lifshitz–Gilbert equation is obtained in the present of spin-polarized current. In the high magnetic field, the deviation of magnetization from the direction of the field is small. Thus, we only consider low-energy excitation. We take spin wave ansatz

$$\boldsymbol{m}=(\delta m_x\boldsymbol{e}_x+\delta m_y\boldsymbol{e}_y)\,{\rm e}^{{\rm i}(kx-\omega t)}+\boldsymbol{e}_z,\tag{33}$$

corresponding to $\psi=\psi_0\,{\rm e}^{{\rm i}(kx-\omega t)}$, where $\psi_0=(\delta m_x+{\rm i}\delta m_y)/2$, and δm_x and δm_y represent the rescaled amplitude of the spin wave. Keeping the linear terms in ψ_0, we obtain the dispersion relation of the spin wave

$$\omega=(1+{\rm i}\alpha)\omega_0[1+l_0''^2(k_{\rm s}-b_{\rm J}M_s/\gamma A)^2],\tag{34}$$

where $\omega_0=\left[\gamma(H_K-4\pi M_s+H_{\rm ext})-b_{\rm J}^2M_s/2\gamma A\right]/\left(1+\alpha^2\right)$, and

$$\left(l_0''\right)^2=16\gamma^2A^2/\left[8\gamma^2M_sA\left(H_K-4\pi M_s+H_{\rm ext}\right)-M_s^2b_{\rm J}^2\right].$$

It is easy to see that the spin-polarized current changes the energy gap. For large current density,

$$j_{\rm e}\geq e/(\hbar P)\sqrt{2AM_s(H_K-4\pi M_s+H_{\rm ext})},$$

the gap vanishes. This means that without other stimulation, such as thermal effects, the spin-polarized current excites spin waves when its density increases beyond a critical value. The Gilbert damping gives energy gap a rescaling and damps the spin wave.

Considering small deviations of magnetization from the equilibrium direction (along the anisotropy axis) corresponding to $m_x^2+m_y^2\ll m_z^2$, or $|\psi|^2\ll 1$, and taking the long-wavelength approximation,[3] we obtain the following nonlinear Schrödinger equation:

$$\begin{aligned}{\rm i}\frac{\partial\psi}{\partial t} &= \frac{\partial^2\psi}{\partial x^2}-\left(1+\frac{H_{\rm ext}}{H_K-4\pi M_s}\right)\psi\\ &\quad +2|\psi|^2\psi+{\rm i}b_{\rm J}\frac{t_0}{l_0}\frac{\partial\psi}{\partial x}.\end{aligned}\tag{35}$$

By means of the Hirota bilinear method,[63] the one- and two-soliton solutions of Eq. (35) are easily to get. The one-soliton solution is $\psi=k_{\rm R}\,{\rm e}^{{\rm i}[\eta_{\rm I}+(1+H_{\rm ext}/(H_K-4\pi M_s))t]}/\cosh[\eta_{\rm R}+C_{\rm D}/2]$, where $\eta=k[x+(b_{\rm J}t_0/l_0-{\rm i}k)t]$, ${\rm e}^{C_{\rm D}}={\rm e}^{2|\lambda_{\rm D}|}/(4k_{\rm R}^2)$, the suffices R and I denote the real and imaginary parts, and k is an arbitrary complex parameter and can be determined by the initial soliton location and amplitude. From ψ, we obtain the solution of magnetization,

$$\begin{aligned}m_x &= \frac{2k_{\rm R}}{\Delta}\cos\left[\eta_{\rm I}+(1+\frac{H_{\rm ext}}{H_K-4\pi M_s})t\right]\cosh\left[\eta_{\rm R}+\frac{C_{\rm D}}{2}\right],\\ m_y &= \frac{2k_{\rm R}}{\Delta}\sin\left[\eta_{\rm I}+\left(1+\frac{H_{\rm ext}}{H_K-4\pi M_s}\right)t\right]\cosh\left[\eta_{\rm R}+\frac{C_{\rm D}}{2}\right],\\ m_z &= 1-\frac{2k_{\rm R}^2}{\Delta},\end{aligned}\tag{36}$$

where $\Delta=\cosh^2(\eta_{\rm R}+C_{\rm D}/2)+k_{\rm R}^2$.

This one-soliton solution represents a 2π domain wall which is the bound state of double π wall.[64] The height of the soliton is rescaling magnetization. The velocity of wall is $V=-b_{\rm J}-2k_{\rm I}l_0/t_0$. As we can see, the spin-polarized current alters the soliton velocity as $-b_{\rm J}$, proportional to the electron current density. The external field causes the m_x and m_y components of the soliton to oscillate periodically. If applying alternating currents, $b_{\rm J}=Pj_{\rm e}\mu_{\rm B}/(eM_s)\cos(\omega t)$, and the only change to the solutions is $\eta=k[x+b_{\rm J}/(\omega l_0)\sin(\omega t_0 t)-ikt]$. The center of mass of soliton vibrates with the same frequency as alternating currents. Inversely, we consider the effect of nonlinear excitations on the spin-polarized current. In ferromagnetic material with nonuniform magnetization and adiabatic approximation, the spin current density is $\boldsymbol{j}_x=(\mu_{\rm B}/e)Pj_{\rm e}\boldsymbol{m}$.[29] Thus, the one-soliton excitation in nanowire provides spin current with a magnetic pulse like the optical pulse in nonlinear media.

3.2. Bright soliton

When $Q<1$, such as permalloy, the nonlinear solutions of Eq. (31) are different. In this case, the characteristic time and length are $t_0=1/(\gamma(4\pi M_s-H_K))$ and $l_0=\sqrt{2A/((4\pi M_s-H_K)M_s)}$. By the same method, the Landau–Lifshitz–Gilbert equation (31) is transformed into a nonlinear Schrödinger equation

$$\begin{aligned}{\rm i}\frac{\partial\psi}{\partial t} &= \frac{\partial^2\psi}{\partial x^2}+\left(1-\frac{H_{\rm ext}}{4\pi M_s-H_K}\right)\psi\\ &\quad -2|\psi|^2\psi+{\rm i}b_{\rm J}\frac{t_0}{l_0}\frac{\partial\psi}{\partial x}.\end{aligned}\tag{37}$$

The one-soliton solution is $\psi=-\lambda_{\rm B}\,{\rm e}^{{\rm i}\Psi_{\rm B}}[(1+{\rm e}^{{\rm i}\Phi_{\rm B}})+(1-{\rm e}^{{\rm i}\Phi_{\rm B}})\tanh(\zeta/2)]$, where $\Psi_{\rm B}=kx+[2\lambda^2+k^2+kb_{\rm J}t_0/l_0+1+H_{\rm ext}/(4\pi M_s-H_K)]t+\Psi_0$, $\Phi_{\rm B}=\arctan(P_{\rm B}\sqrt{4\lambda_{\rm B}^2-P_{\rm B}^2}/(P_{\rm B}^2-2\lambda_{\rm B}^2))$, and $\zeta_{\rm B}=P_{\rm B}[x-$

$(\sqrt{4\lambda_B^2 - P_B^2} - 2k + b_J t_0/l_0)t] + \zeta_0$, where k, λ_B, P_B, Ψ_0, and ζ_0 are real constants. Thus, the solutions of magnetization are

$$\begin{aligned} m_x &= \frac{\lambda_B}{\Lambda}\left[\cos(\Phi_B + \Psi_B) - \cos\Psi_B \right. \\ &\quad \left. + (\cos(\Psi_B + \Phi_B) + \cos\Psi_B)\tanh(\zeta/2)\right], \\ m_y &= \frac{\lambda}{\Lambda}\left[\sin(\Phi_B + \Psi_B) - \sin\Psi_B \right. \\ &\quad \left. + (\sin(\Psi_B + \Phi_B) + \sin\Psi_B)\tanh(\zeta/2)\right], \\ m_z &= \frac{1}{4\Lambda}\left[4\left(1-\lambda^2\right) + P_B^2 - P_B^2\tanh^2(\zeta/2)\right], \end{aligned} \tag{38}$$

where $\Lambda = \left[4\left(1+\lambda_B^2\right) - P_B^2 + P_B^2\tanh^2(\zeta_B/2)\right]/4$. In this solution, in addition to the change of velocity, spin-polarized current induces the oscillation of m_x and m_y components.

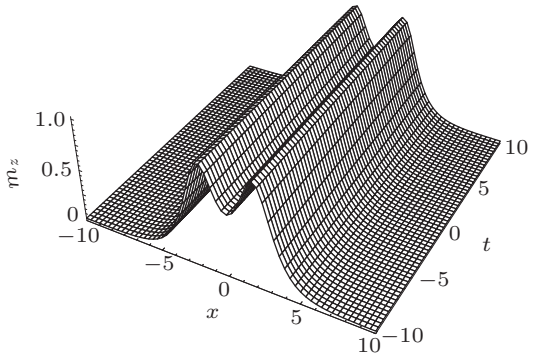


Fig. 11. Two neighbor bright solitons of m_z component with $H_y = 1000$ Oe.[38]

When the external magnetic field deviates from the z axis, in general, the equations cannot be exactly solved.[65] However, some special solutions can be found. For example, we consider the case that $\boldsymbol{H}_{\rm ext} = H_x\boldsymbol{e}_x + H_z\boldsymbol{e}_z$ and $Q < 1$. In the present of spin-polarized current, there exists a dynamic soliton solution

$$\begin{aligned} m_x &= \frac{1 - D^2\cosh^2\xi}{1 + D^2\cosh^2\xi}\cos(\gamma H_z t_0 t), \\ m_y &= \frac{1 - D^2\cosh^2\xi}{1 + D^2\cosh^2\xi}\sin(\gamma H_z t_0 t), \\ m_z &= \frac{2D\cosh\xi}{1 + D^2\cosh^2\xi}, \end{aligned}$$

where $\xi = \sqrt{1 - \gamma t_0 H_x}(x + b_J t_0/l_0 t)$, and

$$D = \sqrt{(\gamma H_x t_0)/(1 - \gamma H_x t_0)}.$$

This solution is plotted in Fig. 11 with the same material parameters as above. The depth and width of trough decrease as H_x increases. The amplitudes of m_x and m_y oscillate with frequency γH_z. When the external field perpendicular to wire's axis vanishes, the magnetization rotates purely in a plane parallel to wire's axis.

3.3. Current driven interaction of spin wave and soliton

In this section, we will investigate the properties of magnetic soliton on a nonlinear spin wave background. It is obvious that $\boldsymbol{m} \equiv (m_x, m_y, m_z) = (0, 0, 1)$ forms the ground state of system, and two types of nonlinear excited states, i.e., spin wave solution and magnetic soliton, are admitted for Eq. (32). When the magnetic field is high enough, the deviation of magnetization from the ground state is small for two types of excited states. In this case, we can make a reasonable transformation

$$\psi = m_x + \mathrm{i}m_y, \quad m_z = \sqrt{1 - |\psi|^2}. \tag{39}$$

Substituting the above equations into Eq. (32), we obtain

$$\begin{aligned} \mathrm{i}\frac{\partial\psi}{\partial t} &= m_z\frac{\partial^2}{\partial x^2}\psi - \psi\frac{\partial^2}{\partial x^2}m_z - \alpha\left(m_z\frac{\partial}{\partial t}\psi - \psi\frac{\partial}{\partial t}m_z\right) \\ &\quad + \mathrm{i}\frac{b_J t_0}{l_0}\frac{\partial}{\partial x}\psi - \left(m_z + \frac{H_{\rm ext}}{H_K - 4\pi M_s}\right)\psi. \end{aligned} \tag{40}$$

It is easy to get two solutions of Eq. (40): one is $\psi = 0$, corresponding to the ground state $\boldsymbol{m} = (0, 0, 1)$, and the other is bulk spin wave excitations, $\psi = A_c\,\mathrm{e}^{\mathrm{i}(-k_c x + \omega_c t)}$, corresponding to the periodic spin current

$$\begin{aligned} m_x &= A_c\cos(-k_c x + \omega_c t), \\ m_y &= A_c\sin(-k_c x + \omega_c t), \\ m_z &= \sqrt{1 - A_c^2}, \end{aligned} \tag{41}$$

where k_c and ω_c are the dimensionless wave number and frequency of spin wave, and the transverse amplitude $A_c \ll 1$. For the attractive interaction, the nonlinear spin waves in ferromagnet with anisotropy lead to the macroscopic phenomena, i.e., the appearance of spatially localized magnetic excited state (magnetic soliton).

In this subsection we want to obtain the soliton solution of magnetization on a nonlinear spin wave background in a uniaxial ferromagnetic nanowire with spin torque. However, equation (40) is not integrable. To our purpose, we consider the case of without damping and the long-wavelength approximation,[3] where the dimensionless wave number $k_c \ll 1$. Keeping only the nonlinear terms of the order of the magnitude of $|\psi|^2\psi$, equation (40) can be simplified as an integrable equation

$$\mathrm{i}\frac{\partial\psi}{\partial t} = \partial_x^2\psi + \frac{1}{2}\psi|\psi|^2 + \mathrm{i}A_J\partial_x\psi - \omega_0\psi, \tag{42}$$

where $\omega_0 = 1 + H_{\rm ext}/(H_K - 4\pi M_s)$ and $A_J = b_J t_0/l_0$. The soliton solutions on the background of the ground state, $\psi = 0$, can be obtained by Hirota methods.[38,63] In order to discuss the properties of soliton solution on the background of spin wave, here we use a straightforward Darboux transformation[66–69] to construct general expressions of soliton solution of Eq. (42).

The main idea of Darboux transformation is that it firstly transforms the nonlinear equation into the Lax representation,

and then in terms of a series of transformations, the soliton solution can be constructed algebraically with an obvious seed solution of the nonlinear equation. Taking the spectral parameter $\lambda = \lambda_1 \equiv \mu_1/2 + \mathrm{i}\nu_1/2$, here μ_1 and ν_1 are real numbers, we obtain the one-soliton solution as

$$\begin{aligned} m_x &= A_\mathrm{c}\cos\varphi + \frac{2\mu_1}{\Delta_1}\left(Q_1\cos\varphi - Q_2\sin\varphi\right), \\ m_y &= A_\mathrm{c}\sin\varphi + \frac{2\mu_1}{\Delta_1}\left(Q_1\sin\varphi + Q_2\cos\varphi\right), \\ m_z &= \sqrt{1-\left(A_\mathrm{c}+\frac{2\mu_1 Q_1}{\Delta_1}\right)^2 - (\frac{2\mu_1 Q_2}{\Delta_1})^2}, \end{aligned} \tag{43}$$

where

$$\begin{aligned} &\varphi = -k_\mathrm{c}x + \omega_\mathrm{c}t, \\ &Q_1 = A_\mathrm{c}L_{1\mathrm{R}}\cosh\theta_1 + \left(|L_1|^2 + \frac{1}{4}A_\mathrm{c}^2\right)\cos\Phi_1, \\ &Q_2 = A_\mathrm{c}L_{1\mathrm{I}}\sinh\theta_1 + \left(|L_1|^2 - \frac{1}{4}A_\mathrm{c}^2\right)\sin\Phi_1, \\ &\Delta_1 = \left(|L_1|^2 + \frac{1}{4}A_\mathrm{c}^2\right)\cosh\theta_1 + A_\mathrm{c}L_{1\mathrm{R}}\cos\Phi_1, \end{aligned}$$

with

$$\begin{aligned} \theta_1 &= 2D_{1\mathrm{R}}x + 2\left(D_1\delta_1\right)_\mathrm{R}t + 2x_0, \\ \Phi_1 &= 2D_{1\mathrm{I}}x + 2\left(D_1\delta_1\right)_\mathrm{I}t - 2\varphi_0. \end{aligned} \tag{44}$$

Here the subscript R and I represent the real part and imaginary part, respectively. The other parameters are $D_1 = \sqrt{(\mathrm{i}k_\mathrm{c}/2+\lambda_1)^2 - A_\mathrm{c}^2/4}$, $L_1 = -\mathrm{i}k_\mathrm{c}/2 - D_1 - \lambda_1$, $\delta_1 = -i2\lambda_1 - k_\mathrm{c} + A_\mathrm{J}$, $x_0 = -\left(\ln|C_2/C_1|\right)/2$, and $\varphi_0 = \left[\arg\left(C_2/C_1\right)\right]/2$, where C_1 and C_2 are arbitrary complex constants.

The solution (43) describes a one-soliton solution for the spin-polarized current in ferromagnetic nanowire embedded in the periodic spin current background (41): i) when $\mu_1 = 0$, the solution (43) reduces to spin wave solution $\psi = A_\mathrm{c}\,\mathrm{e}^{\mathrm{i}(\omega_\mathrm{c}t - k_\mathrm{c}x)}$, where the magnon density is also constant; ii) when the spin wave amplitude and wave number vanish, namely, $A_\mathrm{c} = k_\mathrm{c} = 0$, the solution (43) reduces to the solution in the form

$$\begin{aligned} m_x &= \frac{2\mu_1}{\cosh\theta_1}\cos\left(\Phi_1 + \eta\right), \\ m_y &= \frac{2\mu_1}{\cosh\theta_1}\sin\left(\Phi_1 + \eta\right), \\ m_z &= \sqrt{1 - \frac{4\mu_1^2}{\cosh^2\theta_1}}, \end{aligned} \tag{45}$$

where

$$\begin{aligned} &\theta_1 = \mu_1[x + (2\nu_1 + A_\mathrm{J})t + \frac{2}{\mu_1}x_0], \\ &\Phi_1 = \nu_1\left\{x - \left[\frac{1}{\nu_1}\left(\mu_1^2 - \nu_1^2\right) - A_\mathrm{J}\right]t - \frac{2}{\nu_1}\varphi_0\right\}, \end{aligned}$$

$$\eta = \omega_0 t. \tag{46}$$

The solution (45) is in fact the same as the solution (8) in Ref. [38] (one should notice that the transformation (39) is different from that in Ref. [38]).

The solution (45) indicates that the spatially localized excitation,[64] which is denoted by the transverse amplitude $2\mu_1$, deviates from the ground state $\boldsymbol{m} = (0,0,1)$. The components m_x and m_y precess around the component m_z with the frequency $\Omega_1 = \nu_1^2 - \mu_1^2 + A_\mathrm{J} + \omega_0$, and the soliton solution is characterized by the width $1/\mu_1$, the velocity of soliton center $v_1 = -\left(2\nu_1 + b_\mathrm{J}t_0/l_0\right)$. In addition, the solution ψ_1 represents in fact the static magnetic soliton with three integrals of the motion and the uniform magnon density $|\psi_1|^2 = 2u_1$ along the direction of soliton propagation. The wave number $k_{\mathrm{s},1} = -\nu_1$ and the frequency Ω_1 of the carrier wave are related to the dispersion law $\Omega_1 = k_{\mathrm{s},1}^2 - k_{\mathrm{s},1}A_\mathrm{J} - \mu_1^2 + 1 + H_\mathrm{ext}/\left(H_K - 4\pi M_\mathrm{s}\right)$, which shows that the magnetic field contributes to the precession frequency only. The magnetic soliton energy is thought to be $E_1 = -b_\mathrm{J}^2 t_0^2/\left(2l_0\right)^2 - \mu_1^2 + 1 + H_\mathrm{ext}/\left(H_K - 4\pi M_\mathrm{s}\right) + \frac{1}{2}m^* v_1^2$, where the dimensionless effective mass m^* of soliton is $1/2$.

From Eqs. (45) and (46) we also see that the term b_J can change the velocity and the precessional frequency of soliton on a background of the ground state $\boldsymbol{m} = (0,0,1)$. This case confirms the previous study.[13,38] However, on the background (41) novel properties of Eq. (43) will be described below. The properties of envelope soliton solution (43) are characterized by the width $1/\left(2D_{1\mathrm{R}}\right)$, the wave number $k_\mathrm{s} = -2D_{1\mathrm{I}}$, the initial center position $-x_0/D_{1\mathrm{R}}$, and the envelope velocity $v_1 = -\left(D_1\delta_1\right)_\mathrm{R}/D_{1\mathrm{R}}$. The initial center position of soliton moves $x_0\left(2/\mu_1 - 1/D_{1\mathrm{R}}\right)$ by the spin wave, which offers a new way of controlling the soliton in space.

From the expressions of D_1 and δ_1, we find that the velocity and width of envelope soliton are modulated by the amplitude A_c and wave number k_c of spin wave, as shown in Fig. 12. From Figs. 12(a) and 12(c), we see that absolute value of velocity and the width of envelope soliton become large with increasing A_c. Figure 12(b) shows that the value of k_c near $-\nu_1$ has obvious effect on the velocity of soliton. When $k_\mathrm{c} = -\nu_1$, the width of soliton is maximal, as shown in Fig. 12(d).

From Eq. (44) we can directly see that when $D_{1\mathrm{I}}\delta_{1\mathrm{I}} = \delta_{1\mathrm{R}}D_{1\mathrm{R}}$, the parameter θ_1 depend only on x, which implies that the envelope velocity $-\left(D_1\delta_1\right)_\mathrm{R}/D_{1\mathrm{R}}$ becomes zero, i.e., the soliton is trapped in space by the nonlinear spin wave. It should be noted that this condition can be written as

$$j_\mathrm{e} = \frac{eM_\mathrm{s}}{P\mu_\mathrm{B}}\frac{l_0}{t_0}\left(-\mu_1\frac{D_{1\mathrm{I}}}{D_{1\mathrm{R}}} - \nu_1 + k_\mathrm{c}\right), \tag{47}$$

which is determined by the characteristic velocity l_0/t_0, the amplitude, the wave number of soliton and the nonlinear spin wave, and the parameters $(eM_\mathrm{s}/P\mu_\mathrm{B})$, respectively. From a tedious calculation, we find that when $A_\mathrm{c} \ll$

k_c and $\mu_1 \ll \nu_1$, the condition in Eq. (47) reduces to $j_e \approx -2\nu_1 (l_0/t_0)(eM_s/P\mu_B)$. When the amplitude of spin wave vanishes, namely, $A_c = 0$, the trapping condition in Eq. (47) reduces to $j_e = -2\nu_1 (l_0/t_0)(eM_s/P\mu_B)$, which is determined by the characteristic velocity l_0/t_0, the soliton wave number ν_1, and the parameters $(eM_s/P\mu_B)$. These results show that the background has almost no effect on the trapping condition in the special case $A_c \ll k_c$ and $\mu_1 \ll \nu_1$. For the materials of Co_3Pt alloy films[61] which has high perpendicular anisotropy, we chose $H_K = 1\times10^4$ Oe, $A = 1.0\times10^{-6}$ erg/cm, $4\pi M_s = 1\times10^2$ Oe, $\gamma = 1.76\times10^7$ Oe$^{-1}\cdot$s^{-1}, $P = 0.35$, and the dimensionless parameters $k_c = 0.05$, $A_c = 0.02$, $\nu_1 = -0.12$, and $\mu_1 = 0.1$. The critical electric current trapping soliton is $j_e = 1.867\times10^4$ A/cm^2. It is very important to point out that from Eqs. (43) and (19), and expressions of δ_1, the term b_J changes not only the velocity, but also the frequency affecting soliton energy. This property trapping the soliton in space by the nonlinear spin wave is characterized by the spatial and temporal period along the direction of soliton propagation, $x = -(D_1\delta_1)_R t/D_{1R} - x_0/D_{1R}$, denoted by $\pi(D_1\delta_1)_R/\left[\delta_{1I}\left(D_{1R}^2+D_{1I}^2\right)\right]$ and $\pi D_{1R}/\left[\delta_{1I}\left(D_{1R}^2+D_{1I}^2\right)\right]$, respectively.

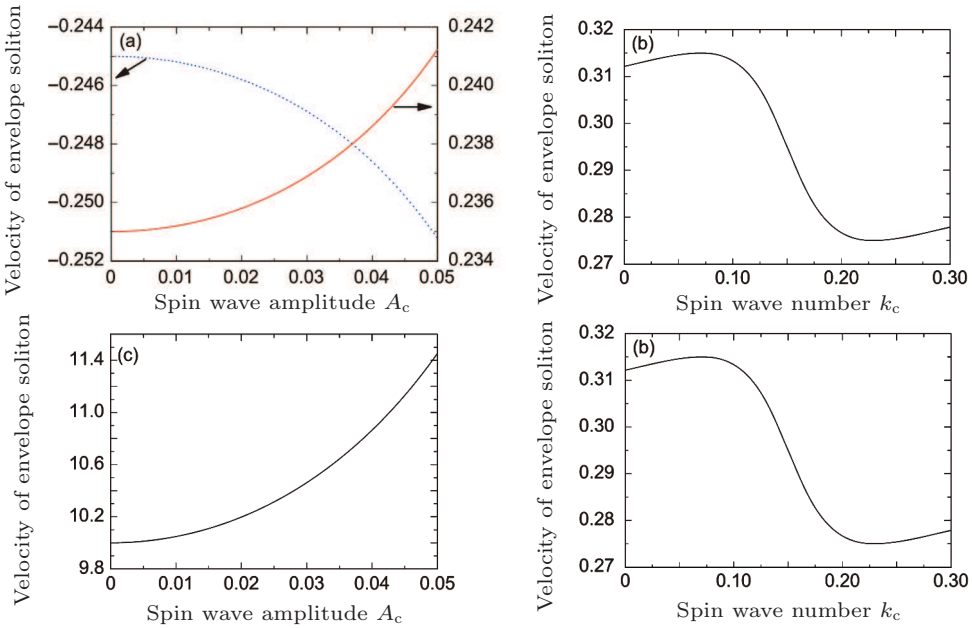


Fig. 12. Velocity and width variety of soliton solution for magnetization versus the amplitude A_c and wave number k_c of spin wave, respectively. The parameters are $\mu_1 = 0.1$, $l_0 = 2\times10^{-8}$ cm, $t_0 = 5.7392\times10^{-12}$ s, and $b_J = 52$ cm/s. (a) Velocity versus amplitude A_c, $k_c = 0.1$, and $\nu_1 = -0.12$ (red line); $k_c = -0.1$, and $\nu_1 = 0.12$ (blue dotted line). (b) Velocity versus spin wave number k_c, $A_c = 0.06$, and $\nu_1 = -0.15$. (c) Width versus amplitude A_c, $k_c = -0.1$, and $\nu_1 = 0.12$. (d) Width versus spin wave number k_c, $A_c = 0.06$, and $\nu_1 = -0.15$.[72]

In order to explain some novel properties of solution (43) we discuss the special case $k_c = -\nu_1$ and analyze two representative situations in detail: (i) amplitude A_c exceeds the half of the transverse amplitude $2\mu_1$ of soliton; (ii) amplitude A_c is smaller than the half of transverse amplitude $2\mu_1$ of soliton, which implies $A_c, \mu_1 > 0$.

(i) In the case of $\mu_1^2 < A_c^2$, the solution (43) reduces to

$$\begin{aligned} m_x &= R_1' \cos\varphi - R_2' \sin\varphi, \\ m_y &= R_1' \sin\varphi + R_2' \cos\varphi, \\ m_z &= \sqrt{1 - A_c^2 - \frac{\zeta_1 (A_c \cosh\theta_1 \cos\Phi_1 - \mu_1)}{(A_c \cosh\theta_1 - \mu_1 \cos\Phi_1)^2}}, \end{aligned} \tag{48}$$

where φ is given by Eq. (44), and the other parameters are determined by $\zeta_1 = 4\mu_1\kappa_1^2$, $\kappa_1 = \sqrt{A_c^2 - \mu_1^2}$, $R_1' = -A_c + 2\kappa_1^2 (\cosh\theta_1)/(A_c\cosh\theta_1 - \mu_1\cos\Phi_1)$, and $R_2' = -2\mu_1\kappa_1 (\sinh\theta_1)/(A_c\cosh\theta_1 - \mu_1\cos\Phi_1)$, with

$$\begin{aligned} \theta_1 &= \mu_1\kappa_1 t + 2x_0, \\ \Phi_1 &= \kappa_1 (x - v_1 t - 2\varphi_0/\kappa_1). \end{aligned} \tag{49}$$

A simple analysis of Eq. (49) reveals that the solution (48) is periodic in the space coordinate, denoted by $2\pi/\kappa_1$, and aperiodic in the temporal variable, as shown in Fig. 13. From Fig. 13 we can see that the background becomes unstable, therefore the solution (48) can be considered as describing the modulation instability process.[69] Along the propagation direction of soliton, the expression of m_z has a maximum $m_z = 1$, at $\cos\Phi_1 = \left(2\mu_1^2 - A_c^2\right)/\mu_1 A_c$ when $A_c^2/4 < \mu_1^2 < A_c^2$, which shows these points are not excited even on the spin wave background, and has a minimum $m_z = [1 - (2\mu_1 + A_c)^2]^{1/2}$ at $\sin\Phi_1 = 0$. When $\mu_1^2 < A_c^2/4$, the expression of m_z has a maximum $m_z = [1 - (2\mu_1 - A_c)^2]^{1/2}$ at $\Phi_1 = 0$, and a minimum $m_z = [1 - (2\mu_1 + A_c)^2]^{1/2}$ at $\Phi_1 = \pi$. These results show that

the linear combination of transverse amplitude of spin wave and magnetic soliton can be obtained in these special cases.

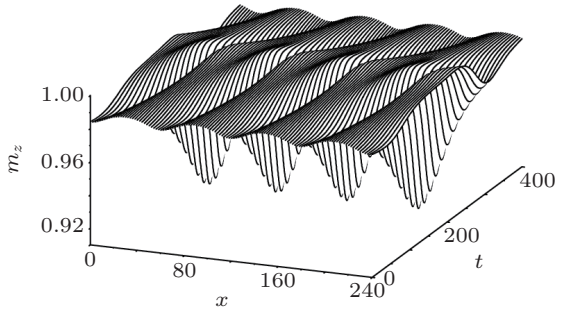


Fig. 13. Evolution of m_z in Eq. (48) with condition of $k_c = -\nu_1$ and $\mu_1^2 < A_c^2$, and the parameters are $\mu_1 = 0.12$, $\nu_1 = -0.1$, $A_c = 0.16$, $b_J = 34.8$ cm/s, $l_0 = 2\times10^{-10}$ m, $t_0 = 5.7392\times10^{-12}$ s, $x_0 = -1.27$, and $\varphi_0 = 0$.[72]

(ii) In the case of $\mu_1^2 > A_c^2$, the solution (43) reduces to

$$\begin{aligned} m_x &= R_1\cos\varphi - R_2\sin\varphi, \\ m_y &= R_1\sin\varphi + R_2\cos\varphi, \\ m_z &= \sqrt{1 - A_c^2 - \frac{\zeta_2(\mu_1 - A_c\cosh\theta_1\cos\Phi_1)}{(\mu_1\cosh\theta_1 - A_c\cos\Phi_1)^2}}, \end{aligned} \tag{50}$$

where

$$\begin{aligned} &\zeta_2 = 4\mu_1\kappa_2^2, \quad \kappa_2 = \sqrt{\mu_1^2 - A_c^2}, \\ &R_1 = -A_c + \frac{2\kappa_2^2\cos\Phi_1}{\mu_1\cosh\theta_1 - A_c\cos\Phi_1}, \\ &R_2 = \frac{2\mu_1\kappa_2\sin\Phi_1}{\mu_1\cosh\theta_1 - A_c\cos\Phi_1}, \\ &\theta_1 = \kappa_2\left(x - v_1 t + 2x_0/\kappa_2\right), \\ &\Phi_1 = -\mu_1\kappa_2 t - 2\varphi_0. \end{aligned} \tag{51}$$

From the expressions (50) and (51) we can see the main characteristics of soliton solution: (i) the soliton has the same envelope velocity $v_1 = -\left(2\nu_1 + b_J t_0/l_0\right)$ on both the background of a periodic spin current in Eq. (41) and the ground state background $\boldsymbol{m} = (0,0,1)$; (ii) the amplitude of m_z in Eq. (50) has the temporal periodic oscillation as shown in Fig. 14. A detail calculation shows that the amplitude of m_z in Eq. (50) has a minimum at $\theta_1 = 0$, which is given by

$$m_z = \sqrt{1 - A_c^2 - \frac{4\mu_1\left(\mu_1^2 - A_c^2\right)}{\mu_1 - A_c\cos\Phi_1}}, \tag{52}$$

and has a maximum

$$m_z = \sqrt{1 - \frac{\mu_1^2 A_c^2\sin^2\Phi_1}{\mu_1^2 - A_c^2\cos^2\Phi_1}}, \tag{53}$$

at $\cosh\theta_1 = 2\mu_1/\left(A_c\cos\Phi_1\right) - \left(A_c\cos\Phi_1\right)/\mu_1$.

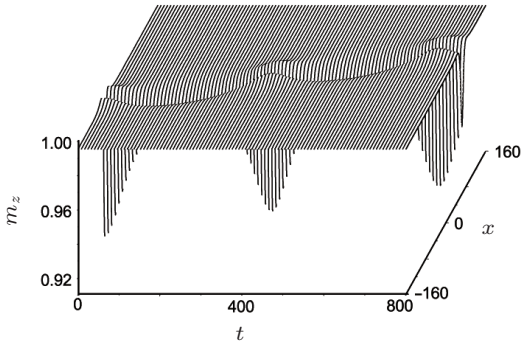


Fig. 14. Evolution of m_z in Eq. (50) with the condition of $k_c = -\nu_1$ and $\mu_1^2 > A_c^2$. The parameters are $\mu_1 = 0.1$, $\nu_1 = -0.08$, $A_c = 0.06$, $b_J = 41.8$ cm/s, $l_0 = 2\times10^{-10}$ m, $t_0 = 5.7392\times10^{-12}$ s, $x_0 = 3$, and $\varphi_0 = 0$.[72]

Figure 15(a) presents the evolution along the propagation direction of the minimum and maximum intensities given by Eqs. (52) and (53) (see, respectively, the dashed and dotted lines), and the spin wave intensity (solid line). The locations of minimum and maximum amplitude (solid and dotted lines, respectively) in the time-space plane are shown in Fig. 15(b). From Fig. 15, it is seen that the narrower the soliton, the sharper the peak, and the deeper the two dips at the wings of the soliton. This feature illustrates the characteristic breather behavior of the soliton as it propagates on the background of a periodic solution for the spin current in ferromagnetic nanowire.

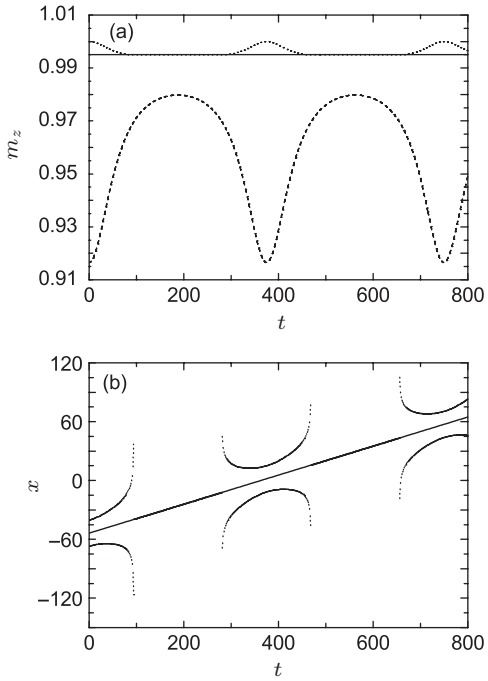


Fig. 15. (a) Evolution of the minimum amplitude of m_z in Eq. (52) (dashed line), the maximum amplitude of m_z in Eq. (53) (dotted line), and the background amplitude of m_z (solid line) in Eq. (41). (b) Location of the minimum amplitude (solid line) and the maximum amplitude (dotted line) in the time-propagation distance plane. The parameters are the same as those in Fig. 14.[72]

3.4. Novel magnetic rogue wave

It is easy to find two basic solutions of Eq. (42). One is $\psi = 0$, which corresponds to the ground state $\boldsymbol{m} = (0,0,1)$.

The other solution is spin wave, i.e., $\psi = A_c e^{i(\omega_c t - k_c x)}$ with ω_c and k_c being the dimensionless frequency and wave number, respectively. In perpendicular anisotropic ferromagnetic nanowire, the interaction of spin waves is attractive and their instability leads to macroscopic phenomena, i.e., the appearance of a spatially localized magnetic excited state (topological or dynamic soliton). As will be shown later, the interaction between spin wave and a dynamic soliton can result in the novel magnetic rogue wave,[70] which can be realized by adjusting the relation of wave number and amplitude for spin wave and a dynamic soliton.

From Eq. (43), we observe that the solution commonly exhibits a breather character and a time periodic modulation for soliton amplitude, which in fact denotes the interaction between the localized process of spin wave background and the periodization process of magnetic soliton. The properties of the soliton solution are characterized by the slope direction $V_\theta \equiv D_{1R}x + (D_1\delta_1)_R t$, the breather propagation velocity $v_q \equiv -(D_1\delta_1)_R/D_{1R}$, and the soliton width $1/D_{1R}$. From the expressions of D_1 and δ_1, we find that the soliton velocity and width are modulated by the amplitude A_c and wave number k_c of spin wave as shown in Figs. 16(a) and 16(d). The absolute values of soliton velocity and soliton width increase with increasing A_c, as shown in Figs. 16(c) and 16(f). Moreover, as the modulation parameter A_c increases continuously, the soliton velocity will be affected mainly by the value of k_c near $-\nu_1$. When $k_c = -\nu_1$, the soliton velocity and width are maximal, as shown in Figs. 16(b) and 16(e). This phenomenon in fact ascribes to magnonic spin-transfer torque[71] which denotes the transfer of spin angular momentum from spin wave background to a dynamic soliton, and it will be discussed elsewhere in detail. On the basis of Eq. (43), as the modulation parameter u_1 approaches A_c, some novel properties will be presented. Magnetic rouge wave solution will be excited in ferromagnetic nanowire, which leads to some fantastic phenomena.

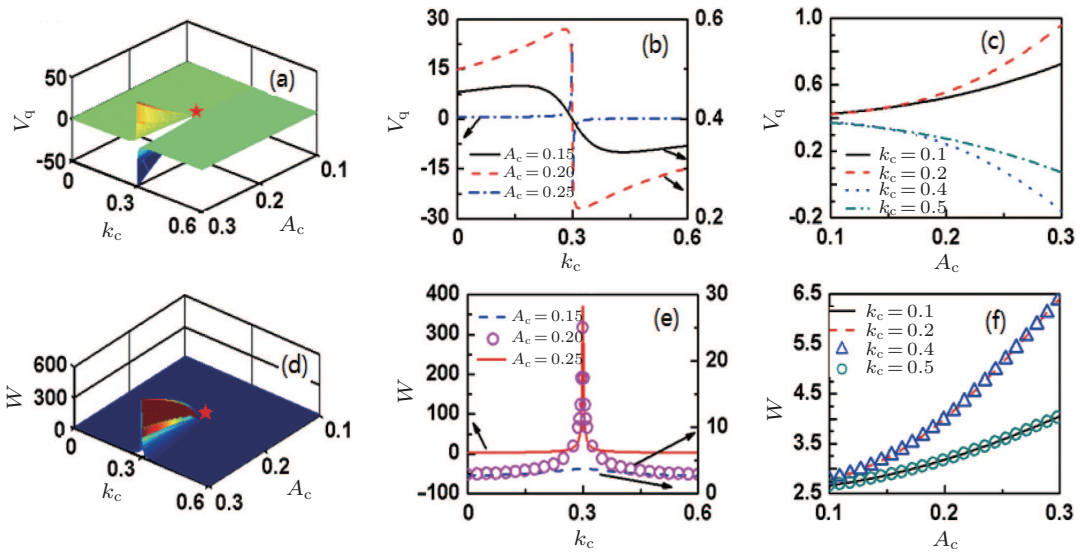


Fig. 16. Breather velocity V_q and width W versus the amplitude A_c and wave number k_c of spin wave. The other parameters are $u_1 = 0.2$, $\nu_1 = -0.3$, and $A_J = 0.2$. (a) and (d) Soliton velocity V_q and width W versus A_c and k_c. The red star signs the location of the rogue wave. (b) and (c) Dependence of velocity on A_c and k_c. (e) and (f) Dependence of velocity on A_c and k_c.[70]

In terms of our previous discussion[72,73] for the solution in Eq. (43), we have known that the critical point $u_1 = A_c$ forms a dividing line between the modulation instability process ($u_1 > A_c$) and the periodization process ($u_1 < A_c$) under the condition of $\nu_1 = -k_c$. There are different physical behaviors when the breather character depends on the modulation parameter u_1 to a different extent, as shown in Fig. 17. Two different asymptotic behaviors are plotted in Fig. 17 in the limit processes $u_1 \to A_c^-$ (and A_c^+) for $\nu_1 = -k_c$, respectively. The former demonstrates a spatial periodic process of a soliton and we observe that the spatial separation of adjacent peak and each peak value increases rapidly as the modulation parameter u_1 approaches A_c, respectively. The latter shows a localized process of the spin-wave background along the slope direction $K_\beta = -(D_1\delta_1)_I/D_{1I}$ for $t_0 = 0$. In this case, the temporal separation of adjacent peaks also increases rapidly as the modulation parameter u_1 approaches A_c, while each peak value decreases rapidly. Even more interesting, in the limit case of $u_1 \to A_c$ (see Ref. [70]), we obtain the novel magnetic rogue wave corresponding to the pentagram sign indicated in Figs. 16(a) and 16(d),

$$\psi = A_c e^{i\varphi}\left[\frac{4\left(1 - itA_c^2\right)}{1 + A_c^2\left(x + \zeta t\right)^2 + t^2 A_c^4} - 1\right], \tag{54}$$

where $\zeta = A_J - 2k_c$. Equation (54) shows the typical rogue

wave feature that the magnons accumulated from spin wave background converge a single hump with the critical amplitude $A_Q = 3A_c$. It implies that the localization wave is captured completely at $x = 0$ and $t = 0$ by spin wave background. As shown in Fig. 18, the realization of magnetic rogue wave in Eq. (54) attributes to the fact that the aggregation of magnons gradually increases as u_1 approaches A_c^-, while decreases gradually when u_1 approaches A_c^+. The temporal localization magnetic rogue wave is excited as $u_1 \to A_c$ with the magnon density peak $|\psi|^2 = 9A_c^2$.

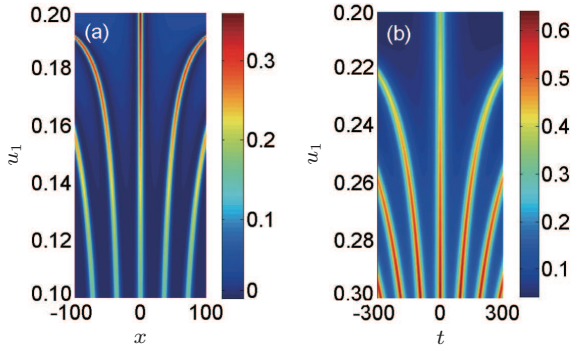


Fig. 17. Evolution of magnetic soliton in the limit processes $u_1 \to A_c^-$ (a) and $u_1 \to A_c^+$ (b). Other parameters are $A_c = 0.2$, $A_J = 0.2$, $k_c = -\nu_1 = 0.003$, and $x_0 = t_0 = 0$.[70]

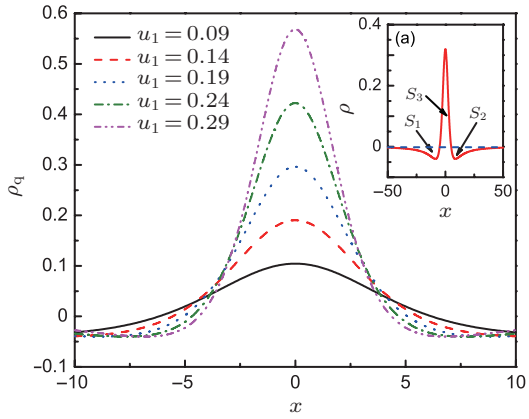


Fig. 18. Magnon density distribution against the background for different parameter u_1, which ranges from 0.09 to 0.29 with a step of 0.05. Inset: Magnon density distribution against the background for the excited formation of magnetic rogue wave. Other parameters are $A_c = 0.2$, $A_J = k_c = 0.1$ and $x_0 = t_0 = 0$.[70]

In order to investigate deeply the properties of magnetic rogue wave in ferromagnetic nanowire, the analysis of the magnon density distribution against the background plays a major role, which is defined by the quantity $\rho_q(x,t) = |\psi(x,t)|^2 - |\psi(x = \pm\infty, t)|^2$. In Fig. 18, we plot the evolution of magnon density distribution for the breather solution in Eq. (43), which ultimately demonstrates the formative mechanism of magnetic rogue wave solution in ferromagnetic nanowire. When the modulation parameter u_1 approaches A_c, the magnons in the background gradually gather toward each individual central part and the envelope becomes sharper. Specially, as shown by the inset (a) in Fig. 18, the critical peak will appear under the condition of $u_1 \to A_c$, i.e., the magnetic rogue wave is excited.

Based on Eq. (54) and the quantity $\rho = |\psi(x,t)|^2 - |\psi(x = \pm\infty, t)|^2$, we obtain the magnon density distribution in a magnetic rogue wave

$$\rho = 8A_c^2 \frac{\Gamma_1 - \Gamma_2}{(\Gamma_1 + \Gamma_2)^2}, \tag{55}$$

where $\Gamma_1 = 1 + t^2 A_c^4$, and $\Gamma_2 = A_c^2 (x + \zeta t)^2$. Equation (55) implies the integral $\int_{-\infty}^{+\infty} \rho(x,t)\,\mathrm{d}x = 0$ for arbitrary time. From the condition of $\rho_Q(\pm 1/A_c, 0) = 0$, we can define the spatial width of the hump part in rogue wave as $2/A_c$. A detail calculation shows that at a fixed time the loss of magnons in background completely transfers to hump, i.e., the area relation $S_1 + S_2 = S_3$. These results clearly illustrate that the generation of magnetic rogue wave with stronger breather character arises mainly from the gathering energy and magnons from the background toward to its central part, and the loss of magnons in background completely transfers to the hump part in magnetic rogue wave.

Another interesting fundamental problem is how rogue wave gathers magnons and energy toward its central part from the background. This can be explained by the quantity $\delta(x,t) \equiv \lim_{l_Q \to \pm\infty} |\psi(x,t) - \psi(x = l_\psi, t)|^2$. From Eq. (54) we obtain

$$\delta(x,t) = 16A_c^2 \frac{\Gamma_1}{(\Gamma_1 + \Gamma_2)^2}, \tag{56}$$

which denotes the nonuniform exchange of magnons between rogue wave and background for different spin currents as shown in Fig. 19. From Eq. (56) we find that the spin current can control the accumulation and dissipation rate of magnons, and there is a critical current condition, i.e., $A_{Jc} = 2k_c$. Below the critical current, the magnon exchange decreases with increasing current term A_J. However, the magnon exchange is accelerated with increasing current above the critical value. The roles of spin-transfer torque are completely opposite for the cases where the current is below and above the critical current, as shown in Fig. 19(f). From Figs. 19(a)–19(e), we see that the magnetic rogue wave can be created in the different direction for (x,t) space, which can be ascribed to the nonuniform exchange of magnons between rogue wave and background tuning by the spin-polarized current. When $A_J = 2k_c$, the time of magnon accumulation (or dissipation) attains its maximum. As shown by the inset in Fig. 19(f), i.e., the integral $\xi(x,t) = \int_{-\infty}^{+\infty} \delta(x,t)\,\mathrm{d}x = 8\pi A_c/(1 + t^2 A_c^4)^{1/2}$, the magnons in background accumulate to the central part when $t < 0$. It leads to the generation of a hump with two grooves on the background along the space direction and the critical peak of the hump can occur at $t = 0$. In contrast, when $t > 0$, the magnons in the hump start to dissipate into the background so that the hump gradually decays. The magnetic rogue wave disappears ultimately, and this verifies that the rogue wave is only

one oscillation in temporal localization and displays a unstable dynamic behavior.

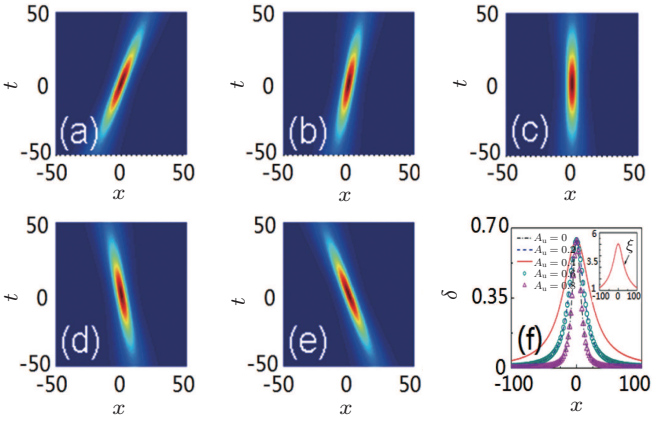


Fig. 19. (a)–(e) Formation region in space (x,t) for magnetic rogue wave with different current. The parameter A_J ranges form 0 to 0.8 with a step of 0.2. (f) Nonuniform exchange of magnons between rogue wave and background for different spin current. The inset in panel (f) denotes the maximal accumulation (or dissipation) process for the critical current value $A_J = 2k_c$. Other parameters are $A_c = 0.2$ and $k_c = 0.2$.[70]

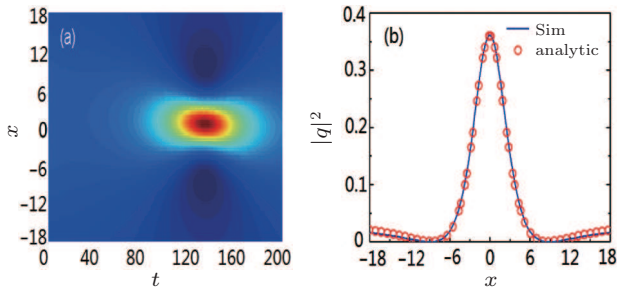


Fig. 20. (a) Numerical evolution of the magnetic rogue wave. (b) Comparison of magnon density between the numerical solution (in solid curve) and ideal solution (in 'o'). Other parameter are $A_c = 0.2$, $u_1 = 0.19$, $x_0 = 0.72$, $A_J = 0.01$, $k_c = 0.2$, and $\omega = 0.2$.[70]

With some specific initial conditions, the excitation of rogue waves can be recovered by means of numerical simulation. In order to understand such a process of magnetic rogue wave, we choose the initial value of solution, which can be approximated by

$$\psi(x,0) = (\rho + \varepsilon\chi\cos\varphi_1)\exp(\mathrm{i}\varphi), \tag{57}$$

where $\rho = \left[2\kappa_1(\kappa_1 - \mathrm{i}u_1) - A_c^2\right]/A_c$, $\varepsilon = \exp(-x_0)$, $\chi = 4\kappa_1 u_1(\kappa_1 - \mathrm{i}u_1)/A_c^2$, and $\varphi_1 = \kappa_1 x$ with $\kappa_1 = \sqrt{A_c^2 - u_1^2}$. By direct numerical simulations, we find that the solution of the initial value problem in Eq. (42) with initial condition (57) can be well described by the solution (54). Figure 20(a) is a result of direct numerical simulation, which shows that a small periodic perturbation with a very small modulation parameter can induce a near-ideal rogue wave localization, whose profile is basically consistent with the ideal theoretical limit solution (54), as shown in Fig. 20(b). As a result, a small initial perturbation with a small modulation can induce the generation and breakup of a near-ideal rogue wave.

4. Ferromagnetic resonance in magnetic trilayers

Since the theoretical prediction of the spin-transfer effects on magnetic multilayers, the research has received significant attention due to the potential applications in data storage and microwave emission. The conservation of angular momentum and the exchange coupling between the conductive electron spin and the local magnetization lead to a spin torque. Compared to the magnetic field-related torque, this current-induced torque has the virtue of localization and can reduce the complexity of the devices. The spin-transfer torque results in a variety of magnetization statics and dynamics, such as magnetization reversal,[74] spin wave excitation,[75] chaos,[76] and ferromagnetic resonance.[77–86]

Ferromagnetic resonance is a powerful tool to study the properties of magnetic multilayers.[87] Usually, it is activated by an RF magnetic field. Now, the spin torque enables us to study current-excited ferromagnetic resonance in magnetic tunnel junctions[77,81,82] and spin valves.[78–80] The ferromagnetic resonance signals are detected by a direct output voltage generated by magneto-resistance effect. Theoretically, several authors predicted[83] or explained[84–86] the current-driven ferromagnetic resonance experiments phenomenologically or microscopically.

So far, the properties in magnetic multilayers with parallel or perpendicular anisotropy have been widely discussed. However, tilted anisotropy also holds some intrigue possibilities to optimize the magnetic configuration. There have been several reports on magnetic films with tilted anisotropy, including the fabrication of tilted-anisotropy films,[88] the effects of anisotropy on ferromagnetic resonance modes,[89,90] and the potential application in high-density magnetic recording.[91–96] Furthermore, tilted anisotropy offers a new means to control the current-driven dynamics in magnetic multilayers,[97–101] for example, optimizing the microwave signal generation,[97] enhancing the spin transfer switching,[98] and the current-related ferromagnetic resonance.[99–101] In addition to current, different anisotropy can also be used to control the ferromagnetic resonance properties.

In light of recent experiments on magnetic multilayers with a perpendicular analyzer,[78,98,102,103] we perform a theoretical study on the current-driven ferromagnetic resonance in the magnetic trilayers with a tilted polarizer and a perpendicular analyzer. By linearizing the Landau–Lifshitz–Gilbert–Slonczewski[8] equation, we obtain the expression of output voltage for arbitrary anisotropy in the free and pinned layers. Then, we apply this result to the case of perpendicular analyzer and achieve the ferromagnetic resonance spectra. In addition, we reveal the dependence of the equilibrium location, the res-

onant linewidth, and the resonant frequency on the direct current density and the direction of pinned-layer magnetization.

4.1. Ferromagnetic resonance in a perpendicular-analyzer magnetic trilayer

As depicted in Fig. 21, we consider a magnetic trilayer with two ferromagnetic metallic layers separated by a nonmagnetic metallic or insulating spacer. The film lies in the x–y plane and the free-layer easy axis is denoted by $\boldsymbol{n}$. The direction of the pinned-layer magnetization is fixed and different orientations can be chosen by fabrication.[97,98]

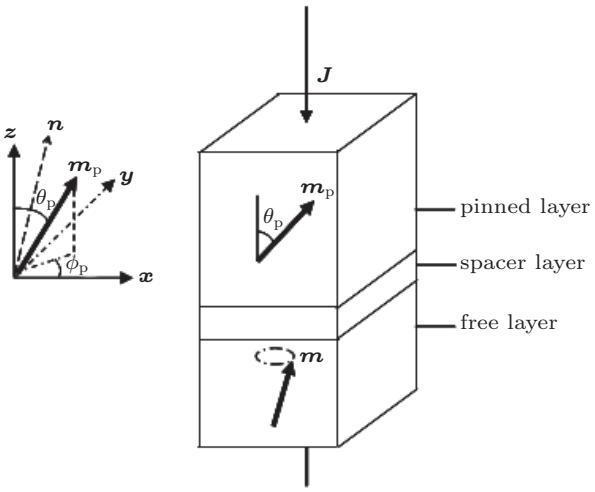


Fig. 21. Schematic drawing of a magnetic trilayer and coordinate system. Applied current flows along the vertical direction of film (z axis).[118]

Considering the spin torque effects, the magnetization dynamics in the free layer can be described by the Landau–Lifshitz–Gilbert–Slonczewski equation,[8]

$$\frac{\partial \boldsymbol{m}}{\partial t} = \frac{\gamma}{M_\mathrm{s}}\boldsymbol{m}\times\frac{\partial E}{\partial \boldsymbol{m}} + \alpha\boldsymbol{m}\times\frac{\partial \boldsymbol{m}}{\partial t} + \gamma a_\mathrm{J}\boldsymbol{m}\times\left(\boldsymbol{m}\times\boldsymbol{m}_\mathrm{p}\right), \quad (58)$$

where γ is the gyromagnetic ratio, α is the Gilbert damping parameter, and M_s is the saturation magnetization of the free layer. $\boldsymbol{m}$ and $\boldsymbol{m}_\mathrm{p}$ are the unit vectors of the free and pinned magnetization, respectively. The magnetic energy includes anisotropic and demagnetization energy, $E = K(1-(\boldsymbol{m}\cdot\boldsymbol{n})^2) + 2\pi M_\mathrm{s}^2\cos^2\theta$, with K being the anisotropy constant, and θ and ϕ the polar and azimuthal angles of $\boldsymbol{m}$. The spin-torque factor a_J is proportional to the current density and dependent on the materials and the angle between the pinned and free magnetization. In general, $a_\mathrm{J} = \hbar g J/(2edM_\mathrm{s})$, where $g = 1/[-4+(3+\boldsymbol{m}\cdot\boldsymbol{m}_\mathrm{p})(1+P)^3/(4P^{3/2})]$, d is the thickness of the free layer, P is the spin polarization, and the current density J takes a positive value when the current flows from the fixed layer to the free one. The current includes direct component and alternating one, i.e., $J = J_\mathrm{dc} + J_\mathrm{ac}\,\mathrm{e}^{\mathrm{i}\omega t}$, where ω is the angular frequency of the alternating current.

It is convenient to transform Eq. (58) into two coupled equations defined by the spherical coordinates,

$$\begin{aligned}
&\frac{\partial\theta}{\partial t} + \alpha\sin\theta\frac{\partial\phi}{\partial t}\\
&= \gamma H_K n_r\left(n_y\cos\phi - n_x\sin\phi\right)\\
&\quad + \gamma a_\mathrm{J}\left(-m_\mathrm{p2}\cos\theta + m_\mathrm{pz}\sin\theta\right),\\
&\sin\theta\frac{\partial\phi}{\partial t} - \alpha\frac{\partial\theta}{\partial t}\\
&= -\gamma\left(H_K n_r n_r' + 2\pi M_\mathrm{s}\sin 2\theta\right) + \gamma a_\mathrm{J} m_\mathrm{p1}, \qquad (59)
\end{aligned}$$

where $n_r = n_x\sin\theta\cos\phi + n_y\sin\theta\sin\phi + n_z\cos\theta$, $n_r' = n_x\cos\theta\cos\phi + n_y\cos\theta\sin\phi - n_z\sin\theta$, $m_\mathrm{p1} = m_{px}\sin\phi - m_{py}\cos\phi$, $m_\mathrm{p2} = m_{px}\cos\phi + m_{py}\sin\phi$, n_x, n_y and n_z are the components of $\boldsymbol{n}$, m_{px}, m_{py}, and m_{pz} are the components of $\boldsymbol{m}_\mathrm{p}$, and $H_K = 2K/M_\mathrm{s}$ denotes the anisotropy field.

Without current, the initial direction of free magnetization is determined by two coupled equations: $n_r(n_y\cos\phi - n_x\sin\phi) = 0$, and $H_\mathrm{k} n_r n_r' + 2\pi M_\mathrm{s}\sin 2\theta = 0$. For parallel analyzer (n_x or n_y = 1), $\boldsymbol{m}$ is along the x direction, i.e., $\theta = \pi/2$ and $\phi = 0$, $\pi/2$, π, or $3\pi/2$. For perpendicular analyzer ($n_z = 1$), if $H_K > 4\pi M_\mathrm{s}$, $\boldsymbol{m}$ is along the z axis, i.e., $\theta = 0$ or π. On the contrary, $\boldsymbol{m}$ lies in the film plane. When applying current, $\boldsymbol{m}$ will deviate from this equilibrium direction and reach a new one (denoted by θ_0 and ϕ_0). Excited by the small alternating current, the free magnetization will oscillate around this new equilibrium. Thus, we can introduce ansatz $\theta = \theta_0 + \Delta\theta\,\mathrm{e}^{\mathrm{i}\omega t}$ and $\phi = \phi_0 + \Delta\phi\,\mathrm{e}^{\mathrm{i}\omega t}$. Substituting this ansatz into Eq. (59) and keeping the linear terms of $\Delta\theta$, $\Delta\phi$, and J_ac, we can obtain the equilibrium equations and the linear solution of $\boldsymbol{m}$. The new equilibrium direction of the free magnetization is determined by

$$\begin{aligned}
&H_K n_{r0} q_2 - a_\mathrm{dc} p_3 = 0,\\
&-\left(H_K n_{r0} n_{r0}' + 2\pi M_\mathrm{s}\sin 2\theta_0\right) + a_\mathrm{dc} p_1 = 0, \qquad (60)
\end{aligned}$$

where $a_\mathrm{dc} = \hbar g_0 J_\mathrm{dc}/(2edM_\mathrm{s})$, $n_{r0} = n_x\sin\theta_0\cos\phi_0 + n_y\sin\theta_0\sin\phi_0 + n_z\cos\theta_0$, $n_{r0}' = n_x\cos\theta_0\cos\phi_0 + n_y\cos\theta_0\sin\phi_0 - n_z\sin\theta_0$, $q_1 = n_x\cos\phi_0 + n_y\sin\phi_0$, $q_2 = n_y\cos\phi_0 - n_x\sin\phi_0$, $p_1 = m_{px}\sin\phi_0 - m_{py}\cos\phi_0$, $p_2 = m_{px}\cos\phi_0 + m_{py}\sin\phi_0$, and $p_3 = p_2\cos\theta_0 - m_{pz}\sin\theta_0$. The expressions for $\Delta\theta$ and $\Delta\phi$ can also be derived as

$$\begin{aligned}
\Delta\theta &= -\frac{p_3 A_{22} + p_1 A_{12}}{A_{22}A_{11} - A_{12}A_{21}}\gamma a_\mathrm{ac},\\
\Delta\phi &= \frac{p_3 A_{21} + p_1 A_{11}}{A_{22}A_{11} - A_{12}A_{21}}\gamma a_\mathrm{ac}. \qquad (61)
\end{aligned}$$

The parameters are set as follows: $A_{11} = \mathrm{i}\omega - \gamma H_K n_{r0}' q_2 - \gamma a_\mathrm{dc}(p_4 + \beta g_0 p_3^2)$, $A_{12} = \mathrm{i}\alpha\omega\sin\theta_0 - \gamma H_K(q_2^2\sin\theta_0 - n_{r0}q_1) - \gamma a_\mathrm{dc}(p_1\cos\theta_0 - \beta g_0 p_1 p_3\sin\theta_0)$, $A_{21} = -\mathrm{i}\alpha\omega + \gamma[H_K(n_{r0}'^2 - n_{r0}^2) + 4\pi M_\mathrm{s}\cos 2\theta] + \gamma a_\mathrm{dc}\beta g_0 p_1 p_3$, and $A_{22} = \mathrm{i}\omega\sin\theta_0 + \gamma H_K q_2(n_{r0}\cos\theta_0 + n_{r0}'\sin\theta_0) - \gamma a_\mathrm{dc}(p_2 + \beta g_0 p_1^2\sin\theta_0)$, where $g_0 = 1/(-4+\beta(3+p_4))$, $p_4 =$

$p_2 \sin\theta_0 + m_{pz}\cos\theta_0$, $\beta = (1+P)^3/(4P^{3/2})$, and $a_{ac} = \hbar g_0 J_{ac}/(2edM_s)$. Because $\Delta\theta$ and $\Delta\phi$ are complex numbers, the response of the free magnetization to the alternating current includes the in-phase and out-of-phase parts.

In real experiments,[77,78] the ferromagnetic resonance signals can be detected by a direct voltage which is generated through the rectification of the alternating current by the time-dependent magnetoresistance. The resistance of the device varies with the precession of free magnetization. Thus, for an applied alternating current,[77]

$$\begin{aligned} R &= R_0 + \frac{\Delta R}{2}\left(1 - \boldsymbol{m}\cdot\boldsymbol{m}_p\right) \\ &= R_0 + \frac{\Delta R}{2}\left(1 - p_4 - \Gamma_1\cos\omega t - \Gamma_2\sin\omega t\right), \end{aligned} \tag{62}$$

where $\Gamma_1 = \mathrm{Re}[p_3\Delta\theta - p_1\Delta\phi\sin\theta_0]$, $\Gamma_2 = \mathrm{Im}[p_3\Delta\theta - p_1\Delta\phi\sin\theta_0]$, R_0 is the resistance of the trilayer when the free and pinned magnetization are parallel, and ΔR is the increase in resistance when they become anti-parallel. Therefore, the output direct voltage can be given by the time-averaged value of $RJ_{ac}S\cos\omega t$ with S being the cross section area of the device,

$$V_{dc} = \frac{1}{T}\int_0^T RJ_{ac}S\cos(\omega t) = \frac{\Delta RJ_{ac}S}{4}\gamma a_{ac}\tau, \tag{63}$$

where τ is dependent on ω, J_{dc}, $\boldsymbol{n}$, and $\boldsymbol{m}_p$,

$$\tau = \mathrm{Re}\left[\frac{p_3\left(p_3A_{22} + p_1A_{12}\right) + p_1\left(p_3A_{21} + p_1A_{11}\right)\sin\theta_0}{A_{22}A_{11} - A_{12}A_{21}}\right]. \tag{64}$$

It is easy to find that the output signal only reflects the in-phase response of the free magnetization to the alternating current. On the basis of Eqs. (63) and (64), we can discuss the current-driven ferromagnetic resonance in magnetic trilayers with arbitrary anisotropy. For instance, $n_x = 1$ corresponds to the trilayers with a parallel analyzer and a tilted polarizer.

In the following discussion, we consider the trilayer with a perpendicular analyzer, namely, $n_z = 1$. In this case, the anisotropy field favors the free magnetization in the vertical direction, while the demagnetizing field favors in-plane. In our calculation, we consider the case that H_K is greater than $4\pi M_s$ (single-axis anisotropy). For perpendicular magnetized devices, the critical current for switching is proportional to $H_K - 4\pi M_s$, which can be adjusted to a low value.[102] Compared with the parallel anisotropy, the perpendicular one has the potential advantage to reduce the energy barrier between the double stable states and the magnetization switching current. Therefore, it is useful to study properties of this devices by ferromagnetic resonance method.

Instead of magnetic field, ferromagnetic resonance can be realized more effectively by adjusting the alternating current frequency due to the wide range of the frequency.[77–79] In the following, we will investigate the frequency-adjusted ferromagnetic resonance for different directions of the pinned magnetization without magnetic field. We take [Co/Ni]×4 multilayers as an illustrative example.[102] The values of related parameters are given as: $\gamma = 1.75\times10^7$ Oe$^{-1}\cdot$s^{-1}, $M_s = 650$ Gs, $H_K = 10154$ Oe, $\alpha = 0.1$, $P = 0.35$, and $d = 3$ nm. For this material, the effective anisotropy field $H_k - 4\pi M_s = 1986$ Oe and along the z axis. The spin-torque parameter a_J has the dimension of magnetic field. For example, with a current density $J = 0.2$ A/μm^2, the value of a_J varies from 538 Oe to 2186 Oe by changing the included angle between the free and pinned magnetization. When the included angle is zero, a_J takes the minimal value, while takes maximum value for 180°. We take $J_{ac} = 0.01$ A/μm^2. The corresponding a_{ac} ranges from 27 Oe to 110 Oe and $a_{ac} \ll (H_K - 4\pi M_s)$.

To avoid the singularity at $\theta = 0°$, we rotate the coordinate system and make the y axis perpendicular to the film plane. In Fig. 22, we plot $V_{dc}/(\Delta RJ_{ac}S)$ as a function of the alternating current frequency for different direct current density. Increasing the direct current from negative to a positive value, the resonant peak turns sharper. However, when the current is greater than about 0.089 A/μm^2, the peak begins to become blunt. This is also indicated in the inset (c), where the linewidth decreases by increasing current from negative to positive value and increases if $J_{dc} > 0.089$ A/μm^2. The spin torque plays dual roles in driving the free magnetization. Depending on the direction of the current and the pinned magnetization, it acts as a damping torque or a precessional one. When the effect of total damping torques (including intrinsic damping) is counterbalanced by the precessional one, the effective damping approaches zero. In this situation, the resonant peak is the sharpest and the linewidth is the least. Thus, the direct current can be used to control the effective damping. The inset (b) indicates that the resonant frequency can be adjusted by the direct current. The frequency reaches the maximum about 34.58 GHz when J_{dc} is 0.003 A/μm^2.

It is interesting to compare the ferromagnetic resonance modes of the parallel and perpendicular analyzers. As depicted in the inset (a) of Fig. 22, we take CoFeB[79] as an example to show the ferromagnetic resonance spectra of the trilayer with a parallel analyzer. When $\theta_p = 60°$ and $\phi_p = 30°$, the resonance peak is asymmetric for a parallel analyzer, while symmetric for a perpendicular one. Because the precession is along a circle for the perpendicular analyzer, the peak is always symmetric in despite of the direction of $\boldsymbol{m}_p$. However, the case is different for parallel analyzer. Due to the effect of demagnetization field, the precession is along an elongated ellipse. When $\boldsymbol{m}_p$ lies in the planes that are perpendicular to the ellipse and with their intersecting lines being one of the two principle axes, it is directed symmetrically with respect to the precessional ellipse and the resonance peak is symmet-

ric. When $\boldsymbol{m}_{\rm p}$ is away from these two planes, the symmetry is destroyed and the peak is asymmetric.

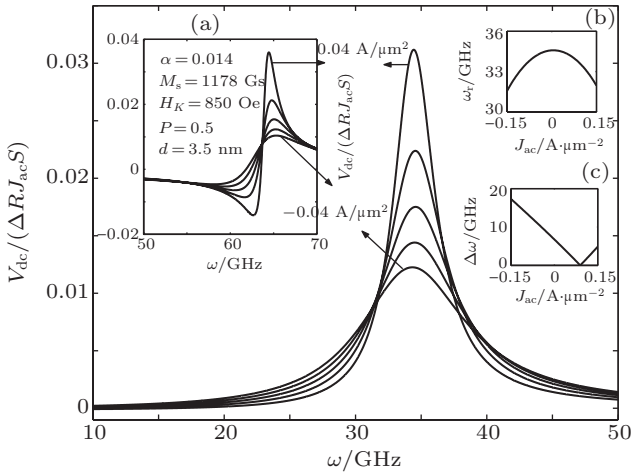


Fig. 22. Ferromagnetic resonance spectra for different dc currents in the case that $\theta_{\rm p} = 60°$ and $\phi_{\rm p} = 30°$. $J_{\rm dc}$ ranges from -0.04 Aμm^2 to 0.04 A/μm^2 in 0.02 A/μm^2 steps. The inset (a) shows the spectra of trilayer with a parallel analyzer. (b) and (c) show the dependence of the resonant frequency and the resonant linewidth on the dc current density.[118]

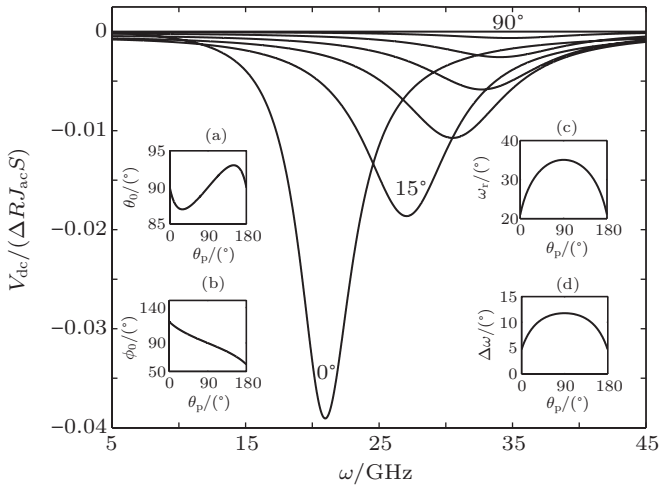


Fig. 23. Ferromagnetic resonance spectra for different directions of the pinned magnetization in the case that $J_{\rm dc} = 0.2$ A/μm^2. $\phi_{\rm p} = 90°$ and $\theta_{\rm p}$ takes values from 0° to 90° in 15° steps. The insets (a) and (b) show the dependence of the equilibrium location on $\theta_{\rm p}$, and (c) and (d) show the dependence of the resonant location and linewidth on $\theta_{\rm p}$.[118]

Figure 23 shows the ferromagnetic resonance curves in a certain direct current and different directions of the pinned magnetization. In the y–z plane, the ferromagnetic resonance peak becomes blunter and blunter with $\theta_{\rm p}$ increasing from 0° to 90°. We find that apart from the magnitude of spin torque, changing the direction of spin torque can also be used to control the ferromagnetic resonance. As indicted in Figs. 23(a) and 23(b), the equilibrium direction of the free magnetization varies with the direction of spin torque. In the parallel configuration, the spin torque is zero and the equilibrium direction is the same as the case without current. The resonant frequency and linewidth can also be adjusted by the direction of spin torque. The inset (c) shows that the resonant frequency is the largest with $\boldsymbol{m}_{\rm p}$ in the film and decreases when the pinned magnetization deviates from this direction. The resonant linewidth exhibits the similar behavior, as indicated in the inset (d). The linewidth is most in the parallel configuration because the spin torque vanishes and the damping is strongest.

4.2. Stability analysis of perpendicular magnetic trilayers

Spin-transfer effects induced by spin-polarized current in spin valve structures have received considerable interest due to promising applications in data storage, information processing, and microwave emission. In general, it can excite some new magnetic states and cause magnetization reversal[74] and precession.[75] According to the symmetry of two interfaces in spin valve structures, there are different dependence of torques on the angle included between the pinned- and free-layer magnetization.

In addition to Slonczewski torque, a field-like spin torque with out-of-plane orientation was proposed.[14] This torque is very small and negligible in symmetric metallic spin valve.[104] However, in magnetic tunnel junction, various experiments found that the relative strength of this torque can reach 10%–100% of the Slonczewski torque.[78,81,105–107] Recent experiments indicated that the microwave power in magnetic tunnel junction oscillators can be enhanced by the field-like spin torque.[108] Theoretical work also showed that this torque has great promise for enhancing the synchronization of magnetic tunnel junction based spin torque oscillators[109] and has a strong impact on switching current density and switching time.[110,111] These studies suggest that the field-like spin torque plays an important role in manipulating magnetization switching and dynamics of nanomagnetic devices although the details of the field-like spin torque are in dispute.

Instead of in-plane anisotropy, magnetic multilayers with perpendicular anisotropy devices have the virtue of high giant magnetoresistance and good thermal stability,[102,103,112] and can lead to fast magnetization reversal.[113,114] Thus, it is significant to study the effect of field-like spin torque on magnetization dynamics in magnetic trilayers with perpendicular anisotropy.

In this subsection, we perform linear stability analysis[99–101,115–122] on the magnetic trilayers with perpendicular anisotropy for both free and fixed layers. By linearizing the Landau–Lifshitz–Gilbert equation including Slonczewski and field-like spin torques and taking stability analysis, several static and dynamic magnetic states are distinguished by adjusting the current and external magnetic field. The behaviors of these states are analyzed by solving temporal evolutive equations. The expression of precession frequency is obtained. In addition, we analyze the effect of field-like spin

torque on the switching current and precession frequency.

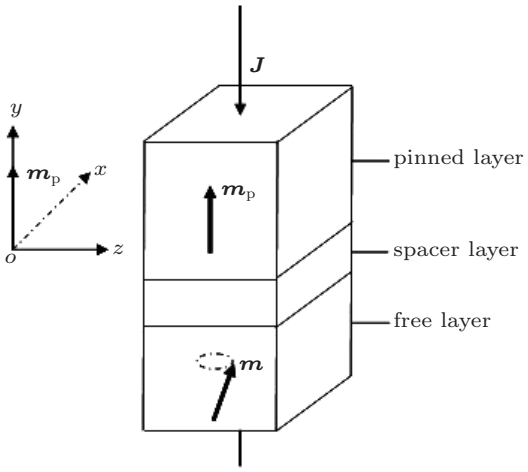


Fig. 24. Schematic drawing of a magnetic trilayer and coordinate system. The easy axis is perpendicular to the film plane and defined as the y direction. The current is applied perpendicularly to the film plane.[119]

As shown in Fig. 24, the magnetic device composed of two ferromagnetic metallic layers separated by a thin normal metallic or insulating spacer is considered. The coordinate system is defined that the film lies in the x–z plane. The magnetic anisotropy in the free layer and pinned layer are all perpendicular to the film. With electrical current flowing perpendicularly through the trilayer, spin polarization takes place in the pinned layer and the magnetization in free layer undergoes a spin-transfer torque generated by current. This torque arises from the exchange coupling between the spins of conductive electrons and local magnetization. Phenomenologically, the magnetization dynamics of free layer can be described by the following dimensionless Landau–Lifshitz–Gilbert equation including the Slonczewski and field-like spin torques,[14,106]

$$\frac{\mathrm{d}\boldsymbol{m}}{\mathrm{d}\tau}-\alpha\boldsymbol{m}\times\frac{\mathrm{d}\boldsymbol{m}}{\mathrm{d}\tau}=-\boldsymbol{m}\times\boldsymbol{h}_{\mathrm{eff}}+\frac{J}{J_{\mathrm{p}}}\frac{[\boldsymbol{m}\times(\boldsymbol{m}\times\boldsymbol{e}_y)]}{1+\lambda_{\mathrm{p}}m_y}+\frac{\beta J}{J_{\mathrm{p}}}\frac{(\boldsymbol{m}\times\boldsymbol{e}_y)}{1+\lambda_{\mathrm{p}}m_y},\tag{65}$$

where $\boldsymbol{m}$ is the unit vector of free-layer magnetization, and α is the Gilbert damping constant. The effective field $\boldsymbol{h}_{\mathrm{eff}}=(\kappa m_y+h_0)\boldsymbol{e}_y$, is the sum of anisotropy field, demagnetizing field, and external magnetic field. $\kappa=h_{\mathrm{k}}-1$, where $h_{\mathrm{k}}=H_K/(4\pi M_{\mathrm{s}})$ and $h_0=H_0/(4\pi M_{\mathrm{s}})$, with H_K being the anisotropy field, H_0 the external magnetic field, and $\boldsymbol{e}_y$ the unit vector along the y direction. The second and third terms on the right of Eq. (65) are the Slonczewski and field-like spin torques, respectively. J is the direct current density and takes a positive value when the current flows from the pinned layer to the free one, $\lambda_{\mathrm{p}}=(1+P)^3/[3(1+P)^3-16P^{3/2}]$, and $J_{\mathrm{p}}=[3(1+P)^3/(2P^{3/2})-8]4\pi deM_{\mathrm{s}}^2/\hbar$, with P being the spin polarization ratio, e the electron charge, $\hbar$ the reduced Planck constant, M_{s} the saturation magnetization of the free layer, and d the film thickness of the free layer. β is the relative strength of field-like torque to Slonczewski one. $\tau=4\pi\gamma M_{\mathrm{s}}t$ is a rescaled variable representing time.

It is convenient to transform Eq. (65) into a pair of coupled differential equations in the polar angle θ and the azimuthal angle ϕ,

$$\begin{aligned}\frac{\partial\theta}{\partial t}+\alpha\frac{\partial\phi}{\partial t}\sin\theta&=(\kappa\sin\theta\sin\phi+h_0)\cos\phi-\frac{J}{J_{\mathrm{p}}}\frac{(\cos\theta\sin\phi+\beta\cos\phi)}{1+\lambda_{\mathrm{p}}\sin\theta\sin\phi},\\-\alpha\frac{\partial\theta}{\partial t}+\sin\theta\frac{\partial\phi}{\partial t}&=-(\kappa\sin\theta\sin\phi+h_0)\cos\theta\sin\phi-\frac{J}{J_{\mathrm{p}}}\frac{(\cos\phi-\beta\cos\theta\sin\phi)}{1+\lambda_{\mathrm{p}}\sin\theta\sin\phi}.\end{aligned}\tag{66}$$

It is apparent from Eq. (65) that $\boldsymbol{m}=\boldsymbol{e}_y$ and $-\boldsymbol{e}_y$ are equilibrium points of magnetization dynamics, i.e., $(\theta_0,\phi_0)=(\pi/2,\pi/2)$ and $(\theta_0,\phi_0)=(\pi/2,3\pi/2)$. Under perturbation, the magnetization oscillates slightly around these equilibrium directions. One can judge the stability of these two equilibrium directions by linear stability analysis.

Substituting $\theta=\pi/2+\delta\theta$ and $\phi=\pi/2+\delta\phi$ into Eq. (66) and keeping the linear terms of $\delta\theta$ and $\delta\phi$, we can obtain the linear differential equations about $\delta\theta$ and $\delta\phi$,

$$\begin{aligned}&\frac{\mathrm{d}}{\mathrm{d}\tau}\delta\theta+\alpha\frac{\mathrm{d}}{\mathrm{d}\tau}\delta\phi\\&=\frac{J}{J_{\mathrm{p}}(1+\lambda_{\mathrm{p}})}\delta\theta-\left[\kappa+h_0-\frac{\beta J}{J_{\mathrm{p}}(1+\lambda_{\mathrm{p}})}\right]\delta\phi,\\&-\alpha\frac{\mathrm{d}}{\mathrm{d}\tau}\delta\theta+\frac{\mathrm{d}}{\mathrm{d}\tau}\delta\phi\\&=\left[\kappa+h_0-\frac{\beta J}{J_{\mathrm{p}}(1+\lambda_{\mathrm{p}})}\right]\delta\theta+\frac{J}{J_{\mathrm{p}}(1+\lambda_{\mathrm{p}})}\delta\phi.\end{aligned}\tag{67}$$

In order to analyze the stability of equilibrium point, we can take $\delta\theta=\Delta\theta\,\mathrm{e}^{\mathrm{i}\omega t}$ and $\delta\phi=\Delta\phi\,\mathrm{e}^{\mathrm{i}\omega t}$ with $\Delta\theta$ and $\Delta\phi$ being the amplitudes. Then, from Eq. (67), we obtain the dispersive equation as

$$\begin{vmatrix}\mu-\dfrac{J}{J_{\mathrm{p}}(1+\lambda_{\mathrm{p}})} & \alpha\mu+\left[\kappa+h_0-\dfrac{\beta J}{J_{\mathrm{p}}(1+\lambda_{\mathrm{p}})}\right]\\ -\alpha\mu-\left[\kappa+h_0-\dfrac{\beta J}{J_{\mathrm{p}}(1+\lambda_{\mathrm{p}})}\right] & \mu-\dfrac{J}{J_{\mathrm{p}}(1+\lambda_{\mathrm{p}})}\end{vmatrix}=0,\tag{68}$$

where $\mu = \mathrm{i}\omega$. Hence, we have

$$\mu = \frac{b \pm \sqrt{\Delta}}{2(1+\alpha^2)}, \tag{69}$$

where $b = 2\left[J(1+\alpha\beta)/\left(J_{\mathrm{p}}(1+\lambda_{\mathrm{p}})\right) - \alpha(\kappa+h_0)\right]$, and $\Delta = -4\left[J(\alpha-\beta)/\left(J_{\mathrm{p}}(1+\lambda_{\mathrm{p}})\right) + \kappa + h_0\right]^2$. As $\Delta < 0$, the equilibrium point $(\theta_0, \phi_0) = (\pi/2, \pi/2)$ is an unstable focus for $b > 0$ and a stable one for $b < 0$. We can obtain the condition for instability as

$$J > J_{\mathrm{c}}^1 = \frac{\alpha(h_0+\kappa)(1+\lambda_{\mathrm{p}})}{(1+\alpha\beta)} J_{\mathrm{p}}. \tag{70}$$

Using the same method, we obtain the condition for the instability of equilibrium point $(\theta_0, \phi_0) = (\pi/2, 3\pi/2)$ as

$$J' < J_{\mathrm{c}}^2 = \frac{\alpha(h_0-\kappa)(1-\lambda_{\mathrm{p}})}{(1+\alpha\beta)} J_{\mathrm{p}}. \tag{71}$$

For many perpendicularly magnetized devices, the interfacial anisotropy provides the perpendicular anisotropy. However, for spin-transport devices, the incorporation of nonmagnetic layers within the magnetic layers affects the spin polarization and leads to high spin-orbit scattering and reduced spin-torque efficiencies. This disadvantage was overcome by the material design of Co/Ni multilayers that combine both high spin polarization and perpendicular magnetic anisotropy.[102] Next we take [Co/Ni]×4 multilayers as an illustrative example[102] and discuss the magnetization dynamics on the basis of Eqs. (70) and (71). The relative parameters used in the calculation are given as follows: the gyromagnetic ratio $\gamma = 1.75 \times 10^7$ Oe^{-1}·s^{-1}, the saturate magnetization $M_{\mathrm{s}} = 650$ G, the anisotropic field $H_{\mathrm{k}} = 10154$ Oe, the Gilbert damping parameter $\alpha = 0.1$, the spin polarization $P = 0.35$, and the thickness of free layer $d = 3$ nm. For this material, $\lambda_{\mathrm{p}} = 0.6048$, $J_{\mathrm{p}} = 1.89$ A/μm^2, and the effective anisotropy field $\kappa = 0.2431$ and along the y axis.

From Eqs. (70) and (71), we find that the instability current is proportional to the external magnetic field. In Fig. 25, we plot the phase diagram in J–β–h_0 parameter space. The blue and red surfaces represent the instability current of equilibrium directions y and $-y$, respectively. By adjusting the current and external magnetic field, several magnetic states can be realized. There are regions that the out-of-plane stable orientations exist. If $J < J_{\mathrm{c}}^1$, the free-layer magnetization is near the y direction, and if $J > J_{\mathrm{c}}^2$ near the $-y$ direction. We denote these regions by 'quasi-P' and 'quasi-AP', respectively. When the current and external field satisfy the condition $J_{\mathrm{c}}^1 < J < J_{\mathrm{c}}^2$, all the equilibrium directions are unstable, the out-of-plane precessional states may emerge, which is denoted by 'OPP'. In other region, the two stable equilibrium directions coexist and are sensitive to the initial state, which is denoted by 'quasi-P or quasi-AP'. The system is in 'quasi-P' state with the initial free-layer magnetization along the y direction, while in 'quasi-AP' with the initial free-layer magnetization along the $-y$ direction.

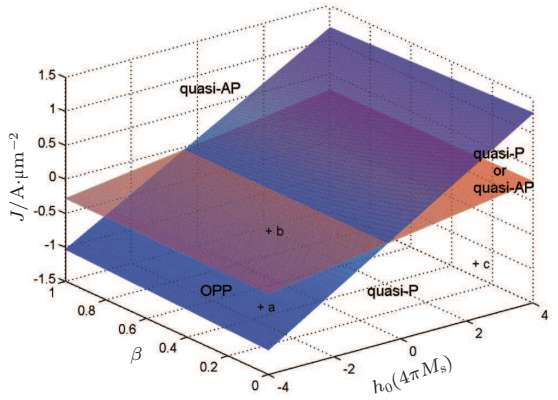


Fig. 25. Phase diagram defined in parameter space spanned by β , h_0, and J. The blue and red surfaces are the instability boundaries of 'quasi-P' and 'quasi-AP' states, respectively.[119]

Depending on the external magnetic field and spin polarized current, one can realize the switching from stable states to precessional ones and the reversal between y and $-y$ orientations. As shown in Fig. 25, for β, h_0, and J located in the region 'OPP', the system enters the out-of-plane precessional state without reference to the initial direction. For β, h_0, and J located in 'quasi-AP' region, the magnetization reversal from 'quasi-P' to 'quasi-AP' happens if the initial direction is along the y axis. For 'quasi-P' region, the reversal from 'quasi-AP' to 'quasi-P' occurs if the initial direction is along the $-y$ axis.

From Fig. 25, one can find that the instability current is weakly dependent on the field-like spin torque. The instability current of quasi-parallel and quasi-antiparallel states are both inversely proportional to β and can be decreased by 10% with β increasing from 0 to 1.

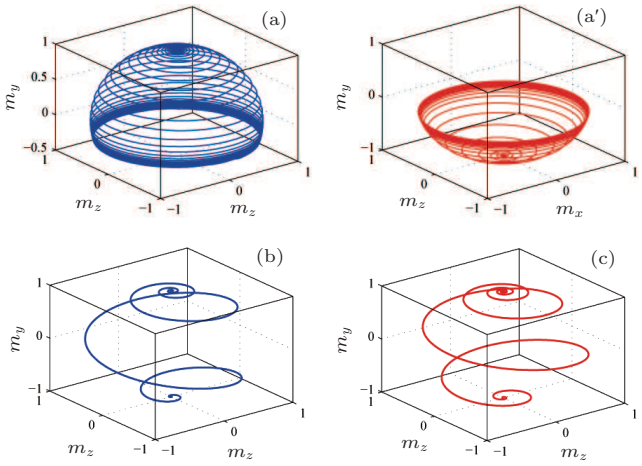


Fig. 26. Dynamic evolutions of the free-layer magnetization for points 'a', 'b', 'c' in Fig. 25. (a) and (a′) Magnetization precession with the initial direction of free-layer magnetization along the y and $-y$ axis, respectively. (b) Magnetization reversal from y to $-y$; (c) magnetization reversal from $-y$ to y.[119]

To confirm the validity of the phase diagram, we pick out three points (a,b,c) from Fig. 25 and plot the dynamic evolutions in Fig. 26. The self oscillations are presented in Figs. 26(a) and 26(a′). The initial states of free-layer magnetization in Figs. 26(a) and 26(a′) are along the y and $-y$ directions, respectively. Figures 26(b) and 26(c) represent the magnetization reversal trajectory.

It must be emphasized that the stability of out-of-plane precession cannot be analyzed by linearizing method. This has been pointed out in Refs. [101] and [122]. We specify the precessional region according to the Poincaré Bendixson theorem.[123,124] As the free-layer magnetization evolves in the (θ, ϕ) state space and is limited within a finite-size region, the static states (fixed points) or limit cycle (self-oscillation) are the only possible final states of the system and chaos is precluded. One can infer that the steady precession must emerge when none of the static solutions are stable.

Considering the rotational symmetry of the problem,[125] we can suppose limit cycle (self-oscillation) solutions $\boldsymbol{m}_0(\tau)$ in the form of magnetization precessing around the y axis with a constant angular velocity,

$$\frac{\mathrm{d}\boldsymbol{m}_0(\tau)}{\mathrm{d}\tau} = \boldsymbol{\omega}\left[\boldsymbol{m}_0(\tau)\times\boldsymbol{e}_y\right]. \tag{72}$$

Substituting this equation into Eq. (58), we find that ω satisfies the following two equations:

$$\omega = -\kappa m_y - h_0 + \frac{\beta J}{J_\mathrm{p}}\frac{1}{1+\lambda_\mathrm{p} m_y}, \tag{73}$$

$$\omega = -\frac{J}{\alpha J_\mathrm{p}\left(1+\lambda_\mathrm{p} m_y\right)}. \tag{74}$$

By excluding m_y from Eqs. (73) and (74), and considering $-1 \le m_y \le 1$, we can obtain the precession frequency of the 'OPP' state as

$$\omega = \frac{\kappa - h_0\lambda_\mathrm{p}}{2\lambda_\mathrm{p}(1+\beta\alpha)} + \frac{\sqrt{\alpha^2 J_\mathrm{p}^2\left(\kappa - h_0\lambda_\mathrm{p}\right)^2 + 4\kappa\alpha J_\mathrm{p}\lambda_\mathrm{p} J(1+\beta\alpha)}}{2\alpha J_\mathrm{p}\lambda_\mathrm{p}(1+\beta\alpha)}. \tag{75}$$

The dependence of frequency on the external magnetic field and current is shown in Fig. 27. The precession frequency increases with increasing external magnetic field. The inset of Fig. 27 shows that the field-like spin torque can diminish the velocity of magnetization precession. With β increasing from 0 to 1, the precession frequency can be decreased more than 10%. The dependence of precession frequency on β can be analyzed qualitatively. From Eq. (58), the influence of the field-like spin torque on precession is related to the directions of effective field and current. Here, the precession exists in the region that $h_\mathrm{eff} = \kappa m_y + h_0 < 0$ and $J < 0$. Thus, the precession produced by the field-like spin torque is opposite to the effective field-induced precession. Because the effective field-induced torque is the leading cause of precession, the frequency decreases with increasing strength of field-like spin torque.

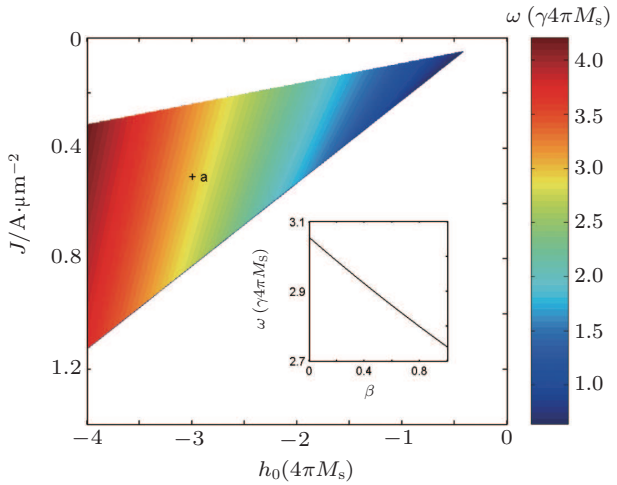


Fig. 27. Precession frequency ω versus J and h_0 for $\beta = 0.1$. The inset shows the dependence of precession frequency ω on β for point 'a'.[119]

4.3. Conclusion

In this paper, we mainly investigate the novel dynamics of magnetization in ferromagnet. In Section 2, we find that the action of adiabatic and non-adiabatic spin torque on motion and distortion of domain wall are different for direct and alternating current. In direct case, the two torques drive wall motion and distortion, respectively. Whereas, the roles are mixed for the alternating current case. Furthermore, in order to depin the domain wall from a potential generated by demagnetization field, an alternating current is preferred to direct one because of decrease in critical current density induced by the resonance. We also obtain the screw-pitch effect and velocity oscillation of domain-wall in ferromagnetic nanowire driven by spin-polarized current. We find that the spin-transfer torque counteracts both the precession driven by the effective field and the Gilbert damping term different from the common understanding. When the spin current exceeds the critical value, the conjunctive action of Gilbert-damping and spin-transfer torque naturally leads to the novel screw-pitch effect characterized by the temporal oscillation of domain wall velocity and width. Driven by spatial and temporal dependence spin-polarized current and magnetic field, we expatiate the formation of domain wall velocity in ferromagnetic nanowire. The equilibrium motion of magnetization is obtained for the cases of below and above the critical current. The domain wall displays the novel nonautonomous helical motion characterized by the coherent rotation without any distortion which is different from the motion driven by the constant current.

Section 3 discusses the properties of dynamic magnetic soliton solutions in uniaxial anisotropic ferromagnetic

nanowire driven by spin-transfer torque. By the Hirota bilinear method, we obtain one and two soliton solutions describing nonlinear magnetization in ferromagnetic nanowire with spin-polarized current. We also study the interaction of a spin wave and one-soliton solution in a uniaxial ferromagnetic nanowire. Our results show that the amplitude of soliton solution has the spatial and temporal period on the spin wave background. The effective mass of soliton is obtained. Moreover, we found that the soliton can be trapped only in space. We also analyze the modulation instability and dark soliton on the spin wave background, showing the characteristic breather behavior of the soliton as it propagates along the ferromagnetic nanowire. At last, we investigated the formative mechanism of magnetic rogue wave and the properties of magnon density in uniaxial anisotropic ferromagnetic nanowire driven by spin-transfer torque. Our results show that the accumulation of energy and magnons toward to its central part plays the main role for the generation of rogue wave with stronger breathing character and rogue wave only appears at the spatial-temporal localization. A novel critical current condition is obtained analytically, and the spin-transfer torque plays a completely opposite role for the case of below and above the critical value.

In Section 4, we have theoretically investigated the current-excited and frequency-adjusted ferromagnetic resonance in magnetic trilayers. A particular case of the perpendicular analyzer reveals that the ferromagnetic resonance curves, including the resonant location and the resonant linewidth, can be adjusted by changing the pinned magnetization direction and the direct current. In some regions defined by the direct current and the pinned magnetization direction, the height of the resonant peak can reach maximum, i.e., resonance linewidth is the smallest. By linearization of Landau–Lifshitz–Gilbert equation, which incorporates Slonczewski and field-like spin torque terms, we plot the phase diagram defined by the current, magnetic field, and relative strength of the two spin torques. There are different magnetic states in the phase diagram, including quasi-parallel and quasi-antiparallel stable states, out-of-plane precession, and bistable states. By adjusting the current and magnetic field, the reversal between parallel and antiparallel orientations and switching from stable states to precessional ones can be realized. The features of different states are shown by the evolution behavior. The precession frequency can be controlled by the current and magnetic field. At last, we analyze the dependence of the critical current and precession frequency on the relative strength of field-like torque to Slonczewski one and find that field-like spin torque can lower instability current and precession frequency. We believe our analysis will provide a useful guide for optimal utilization of spin torque-driven microwave emitting and magnetization reversal in magnetic trilayers with perpendicular anisotropy.

References

[1] Kivshar Y S and Malomed B A 1989 *Rev. Mod. Phys.* **61** 763
[2] Landau L D and Lifshitz E M 1935 *Phys. Z. Sowjetunion* **8** 153
[3] Kosevich A M, Ivanov B A and Kovalev A S 1990 *Phys. Rep.* **194** 117
[4] Mikeska H J and Steiner M 1991 *Adv. Phys.* **40** 191
[5] Gilbert T L 2004 *IEEE Trans. Magn.* **40** 3443
[6] Schryer N L and Walker L R 1974 *J. Appl. Phys.* **45** 5406
[7] Malozemoff A P and Slonczewski J C 1979 *Magnetic Domain Walls in Bubble Material* (New York: Academic)
[8] Slonczewski J C 1996 *J. Magn. Magn. Mater.* **159** L1
[9] Berger L 1996 *Phys. Rev. B* **54** 9353
[10] Tatara G, Kohno H and Shibata J 2008 *Phys. Rep.* **468** 213
[11] Bazaliy Y B, Jones B A and Zhang S C 1998 *Phys. Rev. B* **57** R3213
[12] Tatara G and Kohno H 2004 *Phys. Rev. Lett.* **92** 086601
[13] Li Z and Zhang S 2004 *Phys. Rev. Lett.* **92** 207203
[14] Zhang S, Levy P M and Fert A 2002 *Phys. Rev. Lett.* **88** 236601
[15] Zabusky N J and Kruskal M D 1965 *Phys. Rev. Lett.* **15** 240
[16] Serkin V N, Hasegawa A and Belyaeva T L 2007 *Phys. Rev. Lett.* **98** 074102
[17] Hubert A and Schäferd R 2000 Magnetic Domains: The Analysis of Magnetic Microstructures (New York: Springer)
[18] Ono T, Miyajima H, Shigeto K, Mibu K, Hosoito N and Shinjo T 1999 *Science* **284** 468
[19] Beach G S D, Nistor C, Knutson C, Tsoi M and Erskine J L 2005 *Nat. Mater.* **4** 741
[20] Thomas L, Hayashi M, Jiang X, Moriya R, Rettner C and Parkin S S P 2006 *Nature* **443** 197
[21] Thiaville A, Nakatani Y, Miltat J and Suzuki Y 2005 *Europhys. Lett.* **69** 990
[22] Grollier J, Boulenc P, Cros V, Hamzić A, Vaurès A, Fert A and Faini G 2003 *Appl. Phys. Lett.* **83** 509
[23] Marrows C H 2005 *Adv. Phys.* **54** 585
[24] Parkin S S P, Hayashi M and Thomas L 2008 *Science* **320** 190
[25] Yang J S, Nistor C, Beach G S D and Erskine J L 2008 *Phys. Rev. B* **77** 014413
[26] Wang X R, Yan P and Lu J 2009 *Europhys. Lett.* **86** 67001
[27] Katine J A, Albert F J and Buhrman R A 2000 *Phys. Rev. Lett.* **84** 3149
[28] Arne B, Gerrit E W B and Paul J K 2006 *Phys. Rep.* **427** 157
[29] Li Z and Zhang S 2004 *Phys. Rev. B* **70** 024417
[30] Tsoi M, Jansen A G M, Bass J, Chiang W C, Tsoi V and Wyder P 2000 *Nature* **406** 46
[31] Rezende S M, de Aguiar F M and Azevedo A 2006 *Phys. Rev. B* **73** 094402
[32] Li Z, He J and Zhang S 2005 *J. Appl. Phys.* **97** 10C703
[33] Sun J Z, Monsma D J, Abraham D W, Rooks M J and Koch R H 2002 *Appl. Phys. Lett.* **81** 2202
[34] Tsoi M, Tsoi V, Bass J, Jansen A G M and Wyder P 2002 *Phys. Rev. Lett.* **89** 246803
[35] Chen T Y, Ji Y, Chien C L and Stiles M D 2004 *Phys. Rev. Lett.* **93** 026601
[36] Jiang Y, Yu G H, Wang Y B, Teng J, Ochiai T, Tezuka N and Inomata K 2005 *Appl. Phys. Lett.* **86** 192515
[37] Li Z D, Liang J Q, Li L and Liu W M 2004 *Phys. Rev. E* **69** 066611
[38] He P B and Liu W M 2005 *Phys. Rev. B* **72** 064410
[39] He P B, Xie X C and Liu W M 2005 *Phys. Rev. B* **72** 172411
[40] Koo H, Krafft C and Gomez R D 2002 *Appl. Phys. Lett.* **81** 862
[41] Yamaguchi A, Ono T, Nasu S, Miyake K, Mibu K and Shinjo T 2004 *Phys. Rev. Lett.* **92** 077205
[42] Saitoh E, Miyajima H, Yamaoka T and Tatara G 2004 *Nature* **432** 203
[43] Lim C K, Devolder T, Chappert C, Grollier J, Cros V, Vaur'es A, Fert A and Faini G 2004 *Appl. Phys. Lett.* **84** 2820
[44] Ohe J and Kramer B 2006 *Phys. Rev. Lett.* **96** 027204
[45] Waintal X and Viret M 2004 *Europhys. Lett.* **65** 427
[46] Bocklage L, Krüger B, Eiselt R, Bolte M, Fischer P and Meier G 2008 *Phys. Rev. B* **78** 180405
[47] Hayashi M, Thomas L, Rrettner C, Moriya R and Parkin S S P 2007 *Nat. Phys.* **3** 21
[48] Tretiakov O A, Liu Y and Abanov A 2010 *Phys. Rev. Lett.* **105** 217203
[49] Berger L 1978 *J. Appl. Phys.* **49** 2156
[50] Salhi E and Berger L 1993 *J. Appl. Phys.* **73** 6405
[51] Serkin V N and Hasegawa A 2002 *IEEE J. Quantum Electron.* **8** 418

[52] Li Q Y, Li Z D, Wang S X, Song W W and Fu G S 2009 *Opt. Commun.* **282** 1676
[53] Zhao F, Li Z D, He P B, Li Q Y, and Liu W M 2011 *Eur. Phys. J. B* **84** 197
[54] Sun Z Z and Schliemann J 2010 *Phys. Rev. Lett.* **104** 037206
[55] Goussev A, Robbins J M and Slastikov V 2010 *Phys. Rev. Lett.* **104** 147202
[56] Slonczewski J C 1981 *J. Magn. Magn. Mater.* **23** 305
[57] Munthe-Kaas H 1995 *BIT* **35** 572
[58] Engo K 2000 *BIT* **40** 41
[59] Li Z D, Li Q Y, Wang X R, Liu W M, Liang J Q and Fu G S 2010 *J. Phys.: Condens. Matter* **22** 216001
[60] Lakshmanan M and Nakamura K 1984 *Phys. Rev. Lett.* **53** 2497
[61] Yamada Y, Van Drent W P, Abarra E N and Suzuki T 1998 *J. Appl. Phys.* **83** 6527
[62] Belliard L, Miltat J, Kottler V, Mathet V, Chappert C and Valet T 1997 *J. Appl. Phys.* **81** 5315
[63] Hirota R 1973 *J. Math. Phys.* **14** 805
[64] Liu W M, Wu B, Zhou X, Campbell D K, Chui S T and Niu Q 2002 *Phys. Rev. B* **65** 172416
[65] Takeno S 1984 *Dynamical Problems in Soliton Systems* (Berlin: Springer-Verlag)
[66] Matveev V B and Salli M A 1991 *Springer Series in Nonlinear Dynamics* (Berlin: Springer)
[67] Gu C H, Hu H S and Zhou Z X 1999 *Darboux Transformation in Soliton Theory and its Geometric Applications* (Shanghai: Shanghai Scientific and Technical Publishers) (in Chinese)
[68] Li L, Li Z H, Li S Q and Zhou G S 2004 *Opt. Commun.* **234** 169
[69] Li S Q, Li L, Li Z H and Zhou G S 2004 *J. Opt. Soc. Am. B* **21** 2089
[70] Zhao F, Li Z D, Li Q Y, Wen L, Fu G S and Liu W M 2012 *Ann. Phys.* **327** 2085
[71] Yan P, Wang X S and Wang X R 2011 *Phys. Rev. Lett.* **107** 177207
[72] Li Z D, Li Q Y, Li L and Liu W M 2007 *Phys. Rev. E* **76** 026605
[73] Li Z D, Li Q Y, He P B, Bai Z G and Sun Y B 2007 *Ann. Phys.* **322** 2945
[74] Myers E B, Ralph D C, Katine J A, Louie R N and Buhrman R A 1999 *Science* **285** 867
[75] Kiselev S I, Sankey J C, Krivorotov I N, Emley N C, Schoelkopf R J, Buhrman R A and Ralph D C 2003 *Nature* **425** 380
[76] Lee K J, Deac A, Redon O, Nozi'eres J P and Dieny B 2004 *Nat. Mater.* **3** 877
[77] Tulapurkar A A, Suzuki Y, Fukushima A, Kubota H, Maehara H, Tsunekawa K, Djayaprawira D D, Watanabe N and Yuasa S 2005 *Nature* **438** 339
[78] Sankey J C, Braganca P M, Garcia A G F, Krivorotov I N, Buhrman R A and Ralph D C 2006 *Phys. Rev. Lett.* **96** 227601
[79] Fuchs G D, Sankey J C, Pribiag V S, Qian L, Braganca P M, Garcia A G F, Ryan E M, Li Z P, Ozatay O, Ralph D C and Buhrman R A 2007 *Appl. Phys. Lett.* **91** 062507
[80] Chen W, Beaujour J M L, De Loubens G, Kent A D and Sun J Z 2008 *Appl. Phys. Lett.* **92** 012507
[81] Kubota H, Fukushima A, Yakushiji K, Nagahama T, Yuasa S, Anda K, Maehara H, Nagamine Y, Tsunekawa K, Djayaprawira D D, Watanabe N and Suzuki Y 2008 *Nat. Phys.* **4** 37
[82] Sankey J C, Cui Y T, Sun J Z, Slonczewski J C, Buhrman R A and Ralph D C 2008 *Nat. Phys.* **4** 67
[83] Xi H W, Shi Y M and Gao K Z 2005 *J. Appl. Phys.* **97** 03390
[84] Torresa L, Finocchio G, Lopez-Diaz L, Martinez E, Carpentieri M, Consolo G and Azzerboni B 2007 *J. Appl. Phys.* **101** 09A502
[85] Kupferschmidt J N, Adam S and Brouwer P W 2006 *Phys. Rev. B* **74** 134416
[86] Kovalev A A, Bauer G E W and Brataas A 2007 *Phys. Rev. B* **75** 014430
[87] Farle M 1998 *Rep. Prog. Phys.* **61** 755
[88] Shin S C and Agarwala A K 1988 *J. Appl. Phys.* **63** 3645
[89] Layadi A 1999 *J. Appl. Phys.* **86** 1625
[90] Layadi A 2001 *Phys. Rev. B* **63** 174410
[91] Gao K Z and Bertram H N 2002 *IEEE Trans. Magn.* **38** 3675
[92] Wang J P, Zou Y Y, Hee C H, Chong T C and Zheng Y F 2003 *IEEE Trans. Magn.* **39** 1930
[93] Zou Y Y, Wang J P, Hee C H and Chong T C 2003 *Appl. Phys. Lett.* **82** 2473
[94] Wang J P 2005 *Nat. Mater.* **4** 191
[95] Albrecht M, Hu G, Guhr I L, Ulbrich T C and Boneberg J 2005 *Nat. Mater.* **4** 203
[96] Singh A K, Yin J, Ko H Y Y and Suzuki T 2006 *J. Appl. Phys.* **99** 08E704
[97] Zhou Y, Zha C L, Bonetti S, Persson J and Åermanb J 2008 *Appl. Phys. Lett.* **92** 262508
[98] Sbiaa R, Law R, Tan Ei L and Liew T 2009 *J. Appl. Phys.* **105** 013910
[99] He P B, Li Z D, Pan A L, Wan Q, Zhang Q L, Wang R X, Wang Y G, Liu W M and Zou B S 2008 *Phys. Rev. B* **78** 054420
[100] He P B, Li Z D, Pan A L, Wan Q, Zhang Q L, Wang R X, Wang Y G, Liu W M and Zou B S 2009 *J. Appl. Phys.* **105** 043908
[101] Wang R X, He P B, Li Z D, Pan A L and Liu Q H 2011 *J. Appl. Phys.* **109** 039905
[102] Mangin S, Ravelosona D, Katine J A, Carey M J, Terris B D and Fullerton E E 2006 *Nat. Mater.* **5** 210
[103] Seki T, Mitani S, Yakushiji K and Takanashi K 2006 *Appl. Phys. Lett.* **89** 172504
[104] Urazhdin S, Birge Norman O, Pratt W P and Jr Bass J 2003 *Phys. Rev. Lett.* **91** 146803
[105] Petit S, Baraduc C, Thirion C, Ebels U, Liu Y, Li M, Wang P and Dieny B 2007 *Phys. Rev. Lett.* **98** 077203
[106] Li Z, Zhang S, Diao Z, Ding Y, Tang X, Apalkov D M, Yang Z, Kawabata K and Huai Y 2008 *Phys. Rev. Lett.* **100** 246602
[107] Deac A M, Fukushima A, Kubota H, Maehara H, Suzuki Y, Yuasa S, Nagamine Y, Tsunekawa K, Djayaprawira D D and Watanabe N 2008 *Nat. Phys.* **4** 803
[108] Zeng Z M, Upadhyaya P, Khalili Amiri P, Cheung K H, Katine J A, Langer J, Wang K L and Jiang H W 2011 *Appl. Phys. Lett.* **99** 032503
[109] Zhou Y and Åkerman J 2009 *Appl. Phys. Lett.* **94** 112503
[110] Zhang Z Z, Qiu Y C, Jin Q Y and Liu Y W 2010 *Appl. Phys. Lett.* **97** 172501
[111] Zhou Y 2011 *J. Appl. Phys.* **109** 023916
[112] Meng H and Wang J P 2006 *Appl. Phys. Lett.* **88** 172506
[113] Kent A D, Öyilmaz B and Hel B E 2004 *Appl. Phys. Lett.* **84** 3897
[114] Lee K J, Redon O and Dieny B 2005 *Appl. Phys. Lett.* **86** 022505
[115] Bazaliy Ya B, Jones B A and Zhang S C 2001 *J. Appl. Phys.* **89** 6793
[116] Grollier J, Cros V, Jaffr'es H, Hamzic A, George J M, Faini G, Ben Youssef J, Le Gall H and Fert A 2003 *Phys. Rev. B* **67** 174402
[117] Morise H and Nakamura S 2005 *Phys. Rev. B* **71** 014439
[118] Wang R X, He P B, Liu Q H, Li Z D, Pan A L, Zou B S and Wang Y G 2010 *J. Magn. Magn. Mater.* **322** 2264
[119] Wang R X, Zhao J L, He P B, Gu G N, Li Z D, Pan A L and Liu Q H 2013 *J. Magn. Magn. Mater.* **327** 132
[120] Stiles M D and Miltat J 2006 in *Spin Dynamics in Confined Magntic Structures III* (Ed. Hillebrands B and Thiaville A) (New York: Springer)
[121] Ebels U, Houssameddine D, Firastrau I, Gusakova D, Thirion C, Dieny B and Buda-Prejbeanu L D 2008 *Phys. Rev. B* **78** 024436
[122] Zhou Y, Bonetti S, Zha C L and Åkerman J 2009 *New J. Phys.* **11** 103028
[123] Bertotti G, Serpico C, Mayergoyz I D, Magni A, d'Aquino M and Bonin R 2005 *Phys. Rev. Lett.* **94** 127206
[124] Perko L 1996 *Differential Equations and Dynamical Systems* (New York: Springer)
[125] Bertotti G, Bonin R, Serpico C, d'Aquino M and Mayergoyz I D 2009 *J. Appl. Phys.* **105** 07D104